J. Fluid Mech. (2001), *vol.* 431, *pp.* 371–405. Printed in the United Kingdom

Simulation of normal vortex–cylinder interaction in a viscous fluid

By A. A. GOSSLER AND J. S. MARSHALL

Department of Mechanical Engineering, and Iowa Institute of Hydraulic Research,
The University of Iowa, Iowa City, IA 52242, USA

(Received 20 February 1999 and in revised form 28 September 2000)

A computational study of three-dimensional vortex–cylinder interaction is reported for the case where the nominal orientation of the cylinder axis is normal to the vortex axis. The computations are performed using a new tetrahedral vorticity element method for incompressible viscous fluids, in which vorticity is interpolated using a tetrahedral mesh that is refit to the Lagrangian computational points at each timestep. Fast computation of the Biot-Savart integral for velocity is performed using a box-point multipole acceleration method for distant tetrahedra and Gaussian quadratures for nearby tetrahedra. A moving least-square method is used for differentiation, and a flux-based vorticity boundary condition algorithm is employed for satisfaction of the no-slip condition. The velocity induced by the primary vortex is obtained using a filament model and the Navier–Stokes computations focus on development of boundary-layer separation from the cylinder and the form and dynamics of the ejected secondary vorticity structure. As the secondary vorticity is drawn outward by the vortex-induced flow and wraps around the vortex, it has a substantial effect both on the essentially inviscid flow field external to the boundary layer and on the cylinder surface pressure field. Cases are examined with background free-stream velocity oriented in the positive and negative directions along the cylinder axis, with free-stream velocity normal to the cylinder axis, and with no free-stream velocity. Computations with no free-stream velocity and those with free-stream velocity tangent to the cylinder axis exhibit similar secondary vorticity structures, consisting of a vortex loop (or hairpin) that wraps around the primary vortex and is attached to the cylinder boundary layer at two points. Computations with free-stream velocity oriented normal to the cylinder axis exhibit secondary vorticity structure of a markedly different character, in which the secondary eddy remains close to the cylinder boundary and has a quasi-two-dimensional form for an extended time period.

1. Introduction

A vortex located close to a solid body generates a boundary layer along the body surface that is subject to a favourable pressure gradient on one side of the vortex and an adverse pressure gradient on the other side. Boundary-layer separation in the adverse pressure gradient region leads to ejection of (secondary) vorticity generated on the body into the surrounding fluid. The secondary vorticity interacts with the original (primary) vortex, and can lead to such consequences as vortex rebound from the surface or breakup of the vortex into small-scale turbulence.

Unsteady fluid loading on structures is frequently dominated by vortex–body interaction. Some common examples are the dynamic stall process for accelerated

airfoils, impact of helicopter rotor vortices with following rotor blades or with the vehicle airframe, interaction of an aircraft trailing vortex with a following aircraft, chopping of a pump intake vortex by the turbine blades, and impact of ship or torpedo hull vortices on the propeller blades. Vortex–body interaction is fundamental in the formation and dynamics of juncture vortices, which effect performance of marine and aerodynamic control surfaces and are responsible for scour at the base of bridge pilings. Interaction of turbulent wall-layer vortices with the body surface controls turbulence production in boundary-layer flows by regulating the generation of new coherent structures. Additional applications of vortex–body interaction are described in two recent reviews of the subject by Doligalski, Smith & Walker (1994) and Rockwell (1998).

The present paper is concerned with boundary-layer separation and ejection of secondary vorticity induced by a vortex located near a circular cylinder, where the vortex axis is nominally orthogonal to the cylinder axis and the vortex core radius is much less than the cylinder diameter. This problem is particularly representative of rotorcraft aerodynamic problems, where impact of rotor tip vortices on the vehicle empennage, airframe and tail section during hover and low-speed flight causes strong impulsive forces and moments on the vehicle (Sheridan & Smith 1980; Bi & Leishman 1990; Bi, Leishman & Crouse 1993). Vortex–cylinder interaction is also important in problems such as turbulence–wall interaction in marine cable boundary layers (Neves, Moin & Moser 1994) and unsteady loading in an array of parallel cylinders owing to vortices shed from upstream cylinders, such as occurs in offshore platform risers, groups of tall buildings, and heat exchanger tube bundles (Rockwell 1998). In these latter applications, the relative orientations of the vortex and cylinder axes may range from nearly parallel to nearly orthogonal.

Vortex–body interaction has been studied extensively for two-dimensional flows, and certain of the processes observed in two-dimensional flows are also apparent (in modified form) in three-dimensional vortex–cylinder interaction. Early experimental studies of a vortex pair impinging on a flat wall show that the vortices do not follow the path predicted by inviscid theory, but instead rebound from the wall and rise upwards again after the initial impact (Harvey & Perry 1971; Barker & Crow 1977). Numerical solutions of the two-dimensional Navier–Stokes equations by Peace & Riley (1983) confirm the explanation, originally offered by Harvey & Perry (1971), that this rebound phenomena is caused by secondary vortices that are shed from the wall under the influence of the original vortex pair. A study of two-dimensional boundary-layer development after impulsive introduction of a vortex near a flat wall with uniform free-stream flow is given by Doligalski & Walker (1984). They demonstrate that the existence of a stagnation point at the wall in the inviscid flow solution leads to abrupt boundary-layer separation. Cases without a wall stagnation point in the inviscid solution exhibit more gradual development of boundary-layer separation. Peridier, Smith & Walker (1991*a*, *b*) examine analytically the formation of a singularity in the solution of the unsteady boundary-layer equations in the infinite-Reynolds-number limit for a two-dimensional vortex near a flat wall, and compare the result with numerical solutions for finite Reynolds numbers. Interaction of vortices of both positive and negative signs and of different strengths with a Blasius boundary layer (with negative vorticity) is studied by Luton, Ragab & Telionis (1995). They report that strong negative vortices induce the familiar ejection of (positive) secondary vorticity from the boundary layer, but weaker negative vortices cause only a downstream boundary-layer thickening and do not induce separation of the boundary layer. Positive vortices cause an uplifting of the negative boundary-layer

vorticity upstream of the vortex, again forming a secondary structure of opposite sign to the original vortex. Numerous studies have been performed for axisymmetric vortex ring impact on a flat wall and for two-dimensional vortex interaction with bodies of different shapes, citations to which are given by Rockwell (1998) and Doligalski *et al.* (1994). The main difference between normal vortex–cylinder interaction and the two-dimensional vortex–wall interaction problem discussed above is the effect of wall curvature in a direction nominally tangent to the vortex axis.

Inviscid solutions for normal vortex–cylinder interaction involve bending of the vortex and deformation of the core cross-sectional shape as it nears the cylinder. The inviscid vortex response is governed by two dimensionless parameters. The impact parameter, $I = 2\pi\sigma_0 U/\Gamma$, is the ratio of the free-stream velocity U normal to the cylinder (assuming the body to be fixed) to the maximum vortex swirl velocity $\Gamma/2\pi\sigma_0$, where σ_0 is the initial vortex radius and Γ is the vortex strength. The thickness parameter, $T = D/\sigma_0$, is the ratio of the cylinder diameter D to the vortex core radius. The inviscid bending of a vortex impinging on a circular cylinder is examined by Affes & Conlisk (1993) and Marshall & Yalamanchili (1994) using vortex filament theory. Affes & Conlisk (1993) show that the impinging vortex induces an adverse pressure gradient in the axial direction on one side of the cylinder face. The predicted pressure gradient is reported to agree well with experimental data for the cases examined until the vortex approaches to within about one core radius of the cylinder (Affes *et al.* 1993). Marshall & Yalamanchili (1994) examine vortex bending for different values of the impact and thickness parameters. For thickness parameters of about 5 or greater, the qualitative behaviour of the vortex can be classified as either attractive or repulsive, depending on the value of the impact parameter. For small impact parameters, the flow induced by the cylinder in the presence of the free-stream normal velocity is weak and the vortex initially bends mostly in the spanwise direction in response to its image vorticity. The spanwise deformation leads to a self-induced velocity of the vortex directed towards the cylinder, giving the appearance that the vortex is attracted to the cylinder. For large impact parameters, the flow induced by the cylinder due to the normal free stream is large enough to overcome the vortex self-induced velocity, causing the vortex to bend away from the cylinder. The model used by Marshall & Yalamanchili (1994) includes axial vortex core flow and variable core area, but the change in vortex core area owing to stretching by the cylinder is found to be minor except at high values of the impact parameter and after large amounts of stretching. Inviscid core shape deformation is examined by Krishnamoorthy, Gossler & Marshall (1999) by solution of the vortex–cylinder impact using the full Euler equations (in the velocity–vorticity formulation) for a case with high impact parameter. Their results exhibit only slight core deformation (with maximum aspect of ratio of about 1.5) up to the time of boundary-layer separation, with little effect on the inviscid slip velocity at the cylinder surface. Krishnamoorthy *et al.* (1999) also compare inviscid predictions for vortex bending with experimental data and show that the inviscid solutions cease to be valid shortly after the onset of boundary-layer separation from the cylinder. For cases with high impact parameter, boundary-layer separation occurs when the vortex is much closer to the cylinder than for cases with low impact parameter.

Several experimental studies of vortex–cylinder interaction have been performed that present results for surface pressure variation and vortex trajectory prior to impact with the cylinder. Bi & Leishman (1990) and Bi *et al.* (1993) examine rotor tip–vortex interaction with a cylinder projecting from a body, modelling a helicopter with a long tail boom in low-speed flight. Trajectories of the tip vortices, located using

the shadowgraph technique, are correlated with surface pressure variation, measured by an array of pressure taps along the cylindrical boom. Vortex impingement on the cylinder is found to cause large transient loads on the cylinder and to induce an adverse pressure gradient along the cylinder span. Using a pulsed laser sheet and atomized mineral oil, Brand, Komerath & McMahon (1989) visualize rotor tip vortices impinging upon a cylindrical body at different forward flight speeds. When the vortex moves close enough to the cylinder, it is observed to lose definition, although a weak low-pressure region is still detectable. Liou, Komerath & McMahon (1990) use phase-averaged laser-Doppler velocimetry to detect formation of secondary vortex structures during rotor tip vortex impact on a cylinder, where the vorticity sign within the secondary structures is opposite to that within the incident vortex. A summary of experimental results for rotor wake interaction with a cylinder is given by Kim & Komerath (1995).

Affes, Xiao & Conlisk (1994) use three-dimensional boundary-layer equations to calculate flow along a cylinder subject to forcing by a normal vortex. This investigation is extended by Xiao, Burggraf & Conlisk (1997), who use an interactive boundary-layer theory that accounts for second-order effects of the boundary layer on the inviscid flow. In these studies, the vortex is modelled using inviscid filament theory. The flow is initialized by a line vortex that is introduced impulsively. The vortex is observed to induce a line of separation on the cylinder boundary layer, which is typified by two nodal points at the ends and a saddle point near the midpoint of the separation line. Xiao *et al.* (1997), in calculations with no background free-stream flow, show that the time to separation changes by only about 10% as the Reynolds number is increased by two orders of magnitude (10^6–10^8). The boundary-layer response therefore seems not to be strongly dependent on Reynolds-number variation in this range. Affes *et al.* (1998) compare results of boundary-layer computations and experimental flow visualization for rotor vortex impact on a cylinder.

Krishnamoorthy *et al.* (1999) present flow-visualization results for the evolution of the secondary vorticity after it is ejected from the cylinder, and for the interaction of the secondary vorticity with the primary vortex. These experiments are performed in water using the laser-induced fluorescence (LIF) technique. The core of a vertical intake vortex is dyed red and the boundary layer of a cylinder towed normal to the body is dyed yellow. Flow imaging is performed with horizontal and vertical laser light sheets and with a laser volume. It is found that the time of onset of boundary-layer separation from the cylinder depends strongly on the normal free-stream velocity (via the impact parameter), with separation occurring when the cylinder is many core diameters away from the cylinder for low impact parameters, but not until after the vortex has bent around the cylinder for high impact parameters. At low impact parameters, the tongue of secondary vorticity ejected from the cylinder is observed to roll up into a distinct vortex loop that wraps around the primary vortex (figure 1*a*). At high impact parameters, the vortex is quite close to the cylinder at the time of separation, and the ejected tongue of vorticity appears to have more of a quasi-two-dimensional form as it is drawn outward and wraps around the vortex (figure 1*b*). The response of the primary vortex to a wrapped vortex loop is examined using both flow visualization and direct computation by Krishnamoorthy & Marshall (1998).

Previous research on vortex–cylinder interaction (cited above) provides a clear understanding of the inviscid vortex response to the body, but our conception of the viscous response of the body boundary layer and the subsequent evolution of the ejected boundary-layer vorticity is more ambiguous. Available experimental data on the ejected secondary vorticity comes either from pointwise velocity measurements or

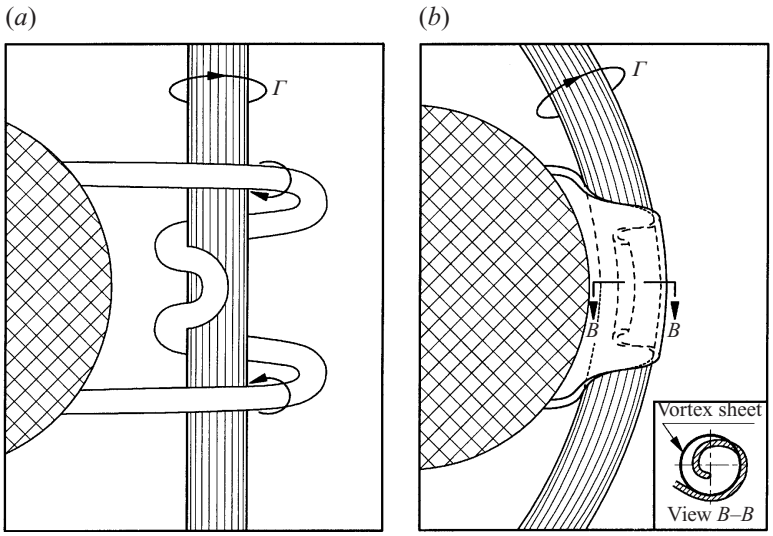

FIGURE 1. Schematic diagrams showing (*a*) loop-like and (*b*) quasi-two-dimensional forms of the ejected secondary vorticity, based on observations from experimental flow visualization (Krishnamoorthy *et al.* 1999).

from flow visualization. The former fail to capture the instantaneous vorticity structure, whereas the latter is, at best, only suggestive of the qualitative flow structure because of the well-known differences between passive scalar and vorticity evolution in three-dimensional flows (e.g. Kida & Takaoka 1994). The only numerical computations of this problem have been based on boundary-layer theory, and hence are not valid past the time of the initial vorticity separation. Many of the main features of the secondary vorticity dynamics remain unclear. For instance, under what external free-stream flow conditions does the secondary vorticity roll up into a loop-like structure, and what is the process that governs the formation of this loop? What is the strength of the secondary vorticity loop in comparison to that of the primary vortex, and how does the loop strength vary along the loop owing to roll up of the ejected vortex sheet? What lengthscales are characteristic of the core radius and leg separation distance of the secondary vortex loop? Does the secondary vortex loop attach directly to the front face of the cylinder, or does it wrap around to the cylinder back face? How does the growth of the secondary vortex loop affect the cylinder surface pressure field and the separation topology?

This paper examines the evolution of the secondary vorticity field during vortex–cylinder interaction with the use of a series of numerical computations of the incompressible Navier–Stokes equations in the vorticity–velocity formulation. To accelerate these computations, the velocity induced by the primary vortex is represented by a vortex filament model. Important parameters characterizing the loop-like structure formed by the secondary vorticity include the loop strength, the peak vorticity, and the separation distance between the loop legs. The study examines how these parameters and the formation of the loop structure itself are affected by background free-stream velocity oriented in the positive and negative spanwise directions and in the direction normal to the cylinder axis. The study also examines the boundary-layer separation topology and surface pressure field and its modification by the ejected secondary vorticity.

An overview of the computational method used in the paper is given in § 2. In § 3, a description is given of the specific problem set-up, computational parameters and validation runs for normal vortex–cylinder interaction. Section 3 also describes the results of the vortex filament computations for the primary vortex and presents a discussion of the limitations of this approximation. Results for impulsive vortex start-up near a cylinder are described in § 4, and the effect of Reynolds number on the ejected secondary vorticity structure in the impulsive start-up case is discussed in § 5. Cases with free-stream velocity in the positive and negative spanwise directions are examined in § 6. A case with free-stream velocity normal to the cylinder, and oriented so as to advect the vortex toward the cylinder, is examined in § 7. Conclusions are presented in § 8.

2. Computational method

The computational method used to evolve the secondary vorticity field solves the Navier–Stokes equations for an incompressible, uniform density fluid in vorticity–velocity form on a set of Lagrangian computational points using a tetrahedral vorticity element (TVE) method (Marshall *et al.* 2000) in conjunction with a filament approximation for the primary vortex. This method requires computational points only within the vorticity-containing parts of the flow and, because it is Lagrangian, it has little or no numerical dissipation and naturally adapts to the evolving vorticity field. The tetrahedral vorticity elements have the advantages, compared to more traditional vortex blob methods, that they can adopt highly anisotropic shapes and they do not carry vorticity over the body surface. These advantages allow the TVE method to compute boundary layer flows more efficiently and to satisfy the body boundary conditions more accurately than previous vortex methods.

In the TVE method, the fluid velocity $\boldsymbol{u}$ is written using the Helmholtz decomposition as the sum of an irrotational part $\boldsymbol{u}_I$, induced by dilatation and boundary conditions at infinity, and a rotational part $\boldsymbol{u}_R$, induced by the vorticity field $\boldsymbol{\omega} \equiv \nabla \times \boldsymbol{u}$ according to the Biot-Savart integral

$$\boldsymbol{u}_R(\boldsymbol{x}, t) = -\frac{1}{4\pi} \int_V \frac{\boldsymbol{r} \times \boldsymbol{\omega}(\boldsymbol{x}', t)}{r^3} \, \mathrm{d}v', \tag{1}$$

with $r \equiv |\boldsymbol{r}| \equiv |\boldsymbol{x} - \boldsymbol{x}'|$. The irrotational part $\boldsymbol{u}_I$ is given by a uniform flow (set by the boundary conditions far from the body) plus the contribution of source panels on the body necessary to maintain the no-penetration condition. In an ideally resolved viscous flow, with no errors arising from discretization of the vorticity field and infinitesimal timestep, the contribution of the source panels would approach zero.

When using a Lagrangian method for a viscous flow calculation, it is convenient to advect the computational points with the sum of the local fluid velocity $\boldsymbol{u}$ and a diffusion velocity $\boldsymbol{v}$, where the diffusion velocity serves to maintain coverage of the diffusing vorticity support by the Lagrangian computational points. The total time derivative of vorticity ($\mathrm{d}_v\boldsymbol{\omega}/\mathrm{d}t$) for a point advected by the sum $\boldsymbol{u} + \boldsymbol{v}$, defined by $\mathrm{d}_v/\mathrm{d}t \equiv \mathrm{d}/\mathrm{d}t + (\boldsymbol{v} \cdot \nabla)$, is given by the vorticity transport equation as

$$\frac{\mathrm{d}_v \boldsymbol{\omega}}{\mathrm{d}t} = (\boldsymbol{\omega} \cdot \nabla)\boldsymbol{u} + (\boldsymbol{v} \cdot \nabla)\boldsymbol{\omega} + \nu \nabla^2 \boldsymbol{\omega}, \tag{2}$$

where ν is the kinematic viscosity.

An expression for diffusion velocity for two-dimensional flows is given by Ogami

& Akamatsu (1991) as

$$\boldsymbol{v} = -\nu\nabla(\ln\omega), \tag{3}$$

where ω is the vorticity magnitude. Equation (3) has the property that the circulation is invariant about any circuit C that is material with respect to the velocity field $\boldsymbol{u}+\boldsymbol{v}$ in a two-dimensional flow (Kempka & Strickland 1993). In three-dimensional flows, (3) does not have this property owing to the effect of curvature of the vortex lines. It is noted, however, that any choice of diffusion velocity is acceptable if it can be demonstrated to adequately cover the vorticity field as it diffuses outward in time. In particular, for high-Reynolds-number laminar flows past a body, most of the viscous diffusion occurs in the boundary layer and the diffusion velocity is required to move points principally in the direction normal to the body surface. For such cases, the diffusion velocity expression (3) maintains coverage of the vorticity field. The adequacy of this expression can also be directly verified from the fact that the vorticity decays gradually at the edges of the tetrahedral mesh connecting the Lagrangian computational points in the solutions presented in §§ 4–7.

The force on an immersed body with surface S and outward unit normal $\boldsymbol{n}$ is given by the sum of the pressure and viscous shear forces as

$$\boldsymbol{F} = -\int_S (p\boldsymbol{n} + \mu\boldsymbol{n}\times\boldsymbol{\omega})\,\mathrm{d}a. \tag{4}$$

A Poisson equation for the stagnation pressure B can be obtained by taking the divergence of the Navier–Stokes equation as

$$\nabla^2 B = \nabla\cdot(\boldsymbol{u}\times\boldsymbol{\omega}), \tag{5}$$

where $B \equiv (p-p_\infty)/\rho + (\kappa-\kappa_\infty)$, $\kappa \equiv \frac{1}{2}\boldsymbol{u}\cdot\boldsymbol{u}$ is the kinetic energy per unit mass, and p_∞ and κ_∞ are constants. Assuming that $B\to 0$ as $r\to\infty$ (for external flow with uniform velocity at infinity), the Green's function solution of (5) for any $\boldsymbol{x}\in V$ can be written as

$$2\pi B(\boldsymbol{x}) - \int_S B\frac{\boldsymbol{n}\cdot\boldsymbol{r}}{r^3}\mathrm{d}a' = -\int_S\left[\nu\frac{\boldsymbol{n}\cdot(\boldsymbol{r}\times\boldsymbol{\omega})}{r^3} + \frac{1}{r}\boldsymbol{n}\cdot\frac{\partial\boldsymbol{u}}{\partial t}\right]\mathrm{d}a + \int_V \frac{\boldsymbol{r}\cdot(\boldsymbol{u}\times\boldsymbol{\omega})}{r^3}\,\mathrm{d}v, \tag{6}$$

where the second term in the surface integral on the right-hand side of (6) vanishes for a fixed body.

Numerical approximation of volume integrals of the convolution form

$$\boldsymbol{g}(\boldsymbol{x}) = \int_V f(\boldsymbol{x}')\boldsymbol{K}(\boldsymbol{x}-\boldsymbol{x}')\,\mathrm{d}v', \tag{7}$$

where $\boldsymbol{K}(\boldsymbol{r}) = \boldsymbol{r}/r^3$, is necessary in order to compute the velocity field from (1) and to compute the volumetric source term in the boundary-integral equation (6) for body surface pressure. In the TVE method, a tetrahedral mesh is used to interpolate the vorticity field in the region surrounding a set of Lagrangian computational points. The computational points are advected by the sum of the local fluid velocity and the diffusion velocity, or

$$\frac{\mathrm{d}\boldsymbol{x}_n}{\mathrm{d}t} = \boldsymbol{u}(\boldsymbol{x}_n,t) + \boldsymbol{v}(\boldsymbol{x}_n,t). \tag{8}$$

A tetrahedral mesh is refitted to these Lagrangian points at each timestep using a fast three-dimensional Delauney triangularization algorithm similar to that of Borouchaki & Lo (1995). The mesh formation procedure starts with a two-dimensional Delauney algorithm to form triangular panels connecting a set of body computational points

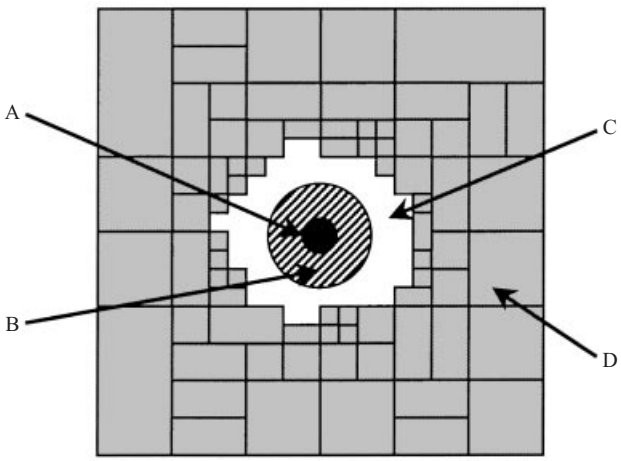

FIGURE 2. Schematic representation showing different methods used to compute velocity (at a point in the centre of the figure): A, analytic surface integration (black); B, 5-point Gaussian quadrature (striped); C, 1-point Gaussian quadrature (white); and D, box-point multipole expansion (grey boxes).

on the surface S, which are then used as the start of an advancing front to form the tetrahedral volume mesh.

Integrals of the form (7) are evaluated using a combination of different methods, illustrated schematically in figure 2, which are selected in an adaptive manner in order to optimize computation speed while maintaining a prescribed accuracy. The selection method examines whether the distance between the 'source' tetrahedron and the 'target' point $\boldsymbol{x}$ exceeds a critical value, which is determined using a modification of the analytical error estimate of Salmon & Warren (1994). The tetrahedra are divided into a set that contributes 'directly' and a set that contributes 'indirectly' to the integral for a given target point, and the direct interaction set is further divided into three subsets.

For the 10–100 tetrahedra closest to the target point, we use an analytical solution that assumes that $f(\boldsymbol{x})$ has a constant value f_m over each tetrahedron, for which case the contribution of the mth tetrahedron can be rewritten as,

$$\int_{V_m} f(\boldsymbol{x}')\boldsymbol{K}(\boldsymbol{x}-\boldsymbol{x}')\,\mathrm{d}v' \cong \sum_{m=1}^{M} f_m \int_{S_m} \frac{\boldsymbol{n}'}{r}\,\mathrm{d}a', \tag{9}$$

where S_m denotes the tetrahedron bounding surface and $\boldsymbol{n}$ is the outward unit normal of S_m. The surface integral in (9) is the same as that which arises in computing the potential due to a source distribution of uniform strength and can be evaluated analytically (Newman 1986) for any piecewise planar surface S_m.

The contribution of tetrahedra at a moderate distance from the target point is computed using a Gaussian quadrature approximation of the form

$$\int_{V_m} f(\boldsymbol{x}')\boldsymbol{K}(\boldsymbol{x}-\boldsymbol{x}')\,\mathrm{d}v' \cong \sum_{l=1}^{G} f(\boldsymbol{\xi}_l)\frac{\boldsymbol{r}_l}{r_l^3} W_l V_m, \tag{10}$$

where the G Gauss points are located at positions $\boldsymbol{\xi}_l$ and have weights W_l. The volume of the mth tetrahedron is denoted by V_m, and $\boldsymbol{r}_l = \boldsymbol{x} - \boldsymbol{\xi}_l$ is the position vector of the target point $\boldsymbol{x}$ relative to the position of the lth Gauss point. Five Gauss

points are used to obtain a cubic approximation for roughly the 10^3 next closest tetrahedra, and one Gauss point is used to obtain a linear approximation for roughly 10^4 more distant tetrahedra. Values of weights and positions of the Gauss points for generalized tetrahedra are given by Zienkiewicz (1977).

For the set of tetrahedra that contributes indirectly to the integral (7), a box-point multipole expansion algorithm is used to accelerate the computation. The computational points in this set are sorted into a tree-like family of rectangular boxes using a Clarke–Tutty (1994) type box generation algorithm. In this algorithm, all computational points are first placed in a single box, and the box is divided in two along the Cartesian direction for which the distance between computational points is greatest. This division process is repeated for each generation of boxes, keeping approximately the same number of points in each box of a given generation, until the number of points in the smallest boxes is less than a specified value (typically about 10). An 'interaction list' is then generated for each target point, which identifies the largest boxes contributing to the integral at that point for which a multipole expansion of the form

$$\boldsymbol{g}_l(\boldsymbol{x}) = \frac{1}{4\pi} \sum_{k=0}^{P} \sum_{n=0}^{P-k} \sum_{m=0}^{P-n-k} \frac{(-1)^{m+n+k}}{m!n!k!} I_{l,mnk} \frac{\partial^{m+n+k}}{\partial x^m \partial y^n \partial z^k} \left(\frac{\boldsymbol{r}_l}{r_l^3} \right) \tag{11}$$

yields an error less than a prescribed value, where P is an integer that specifies the maximum order of the multipole expansion. The benefits of the multipole expansion procedure rapidly diminish when third- and higher-order terms are included for three-dimensional computations, so in the current computations we set $P = 2$. In (11), the subscript l identifies a box with centroid $\boldsymbol{c}_l$ (weighted by computational point positions) and $\boldsymbol{r}_l \equiv \boldsymbol{x} - \boldsymbol{c}_l$ is the position of the target point relative to the box centroid. The term $I_{l,mnk}$ in (11) denotes the moment of the source field $f(\boldsymbol{x})$ contained in the box relative to the box centroid. The moments are computed by associating each tetrahedron with the box tree of one of its nodes, and then analytically integrating a linear approximation for the source distribution $f(\boldsymbol{x})$ multiplied by a given moment arm to obtain the contribution of each tetrahedron to the total box moment. The speed-up in the indirect method is possible because the box moments are independent of the target point (and thus need to be computed only once for each timestep) and the derivatives in (11) depend only on the box centroid positions (and not on the positions of the individual computational points within the box). For the current computations, the indirect procedure is used to account for the contributions of about 90% of the tetrahedra.

Numerical differentiation on the irregularly spaced Lagrangian computational points is necessary to compute the derivatives in the stretching and diffusion terms of the vorticity transport equation (2) and to compute the diffusion velocity from equation (3). Differentiation is performed in the current paper using a three-dimensional extension of the 'moving least-square' algorithm described by Marshall & Grant (1997). We consider a function $f(\boldsymbol{x}, t)$ whose first and second derivatives are desired at a point $\boldsymbol{x}_m$. A local interpolation of $f(\boldsymbol{x}, t)$ in the region around $\boldsymbol{x}_m$ is obtained by fitting a quadratic polynomial $q_m(\boldsymbol{x}, t)$ to the values f_n of $f(\boldsymbol{x}, t)$ on nearby computational points $\boldsymbol{x}_n$ in the form

$$q_m(\boldsymbol{x}, t) = f_m + \sum_{i=1}^{9} F_{m,i} \, W_{m,i}(\boldsymbol{x} - \boldsymbol{x}_m), \tag{12}$$

where $F_{m,i}$ are undetermined coefficients and $W_{m,i}(\boldsymbol{x} - \boldsymbol{x}_m)$ are prescribed linear and

quadratic basis functions. Values of the coefficients $F_{m,i}$ are obtained by minimizing a localized least-square error measure E_m, given by

$$E_m \equiv \sum_{n=1}^{N} L_{mn}[f_n - q_m(\boldsymbol{x}_n, t)]^2, \tag{13}$$

where the 'localization parameter' L_{mn} is set equal to unity for all points n that are nodes of tetrahedra connected to computational point m (the 'first neighbours' of m) or are nodes of tetrahedra that are connected to the first neighbours (the 'second neighbours' of m). For all other points n, the localization function L_{mn} is set to zero. Minimization of E_m with respect to each of the coefficients $F_{m,i}$ yields a 9×9 system of linear equations for $F_{m,i}$. After solving for $F_{m,i}$, the derivatives of f_m can be computed simply by differentiating the polynomial fit (12). As shown by Marshall & Grant (1997), this differentiation method is accurate to second order for uniformly spaced points and has accuracy between first and second order for irregularly spaced points.

The boundary condition for vorticity at the body surface is specified by balancing vorticity associated with surface slip with the total vorticity transported into the fluid volume during the timestep. Vorticity transport into the fluid volume occurs both by viscous diffusion normal to the body surface and by change in the vorticity contained within tetrahedra connected to body computational points in response to a change in the value of the surface vorticity. The former effect was accounted for in the vorticity boundary condition formulation proposed by Koumoutsakos, Leonard & Pépin 1994 using the vortex blob method, but the latter effect is unique to the use of connected tetrahedral elements. The vorticity boundary condition is set by first evaluating the vortex sheet strength $\boldsymbol{\gamma}_m$ associated with the slip velocity $\boldsymbol{\gamma}_m \times \boldsymbol{n}$ at a body point $\boldsymbol{x}_m$. The total vorticity associated with slip at $\boldsymbol{x}_m$ is $\boldsymbol{\gamma}_m \hat{A}_m$, where $\hat{A}_m$ is one-third the area of all triangular panels connected to body point $\boldsymbol{x}_m$. A change $\Delta\boldsymbol{\omega}_m$ in vorticity at $\boldsymbol{x}_m$ causes a change in the total vorticity associated with tetrahedra in the flow of $\hat{V}_m \Delta\boldsymbol{\omega}_m$, where $\hat{V}_m$ is a quarter of the sum of the volume of all tetrahedra attached to body point $\boldsymbol{x}_m$. The amount of vorticity to diffuse into the flow from the region on the body surface with area $\hat{A}_m$ surrounding point $\boldsymbol{x}_m$ during the time interval $(t, t + \Delta t)$ is $-\nu \hat{A}_m \Delta t (\partial\boldsymbol{\omega}/\partial n)|_m$. Balancing the slip vorticity with the vorticity transport from these two mechanisms gives

$$\boldsymbol{\gamma}_m \hat{A}_m = \hat{V}_m \Delta\boldsymbol{\omega}_m - \nu \hat{A}_m \Delta t (\partial\boldsymbol{\omega}/\partial n)|_m. \tag{14}$$

The normal gradient of vorticity to the surface S can be evaluated as a sum of differences of vorticity at the volume and body computational points using the moving least-square formulation. The resulting equation yields an implicit solution for the boundary vorticity, which is solved using a fixed-point iteration procedure. This procedure converges very rapidly, with a relative error of less than 0.01% in 3–4 iterations. Typical values of the surface slip velocity depend on the spatial and temporal resolution. For the computations reported in this paper, the surface slip velocity is maintained with a root-mean-square value of about 0.5% and maximum slip of about 2%, of the maximum velocity outside the boundary layer.

3. Problem set-up

A summary of the computational cases for normal vortex–cylinder interaction is given in table 1, which includes two different vortex Reynolds numbers, $Re = \Gamma/\nu$, and four different free-stream conditions. The initial vortex orientation relative to the

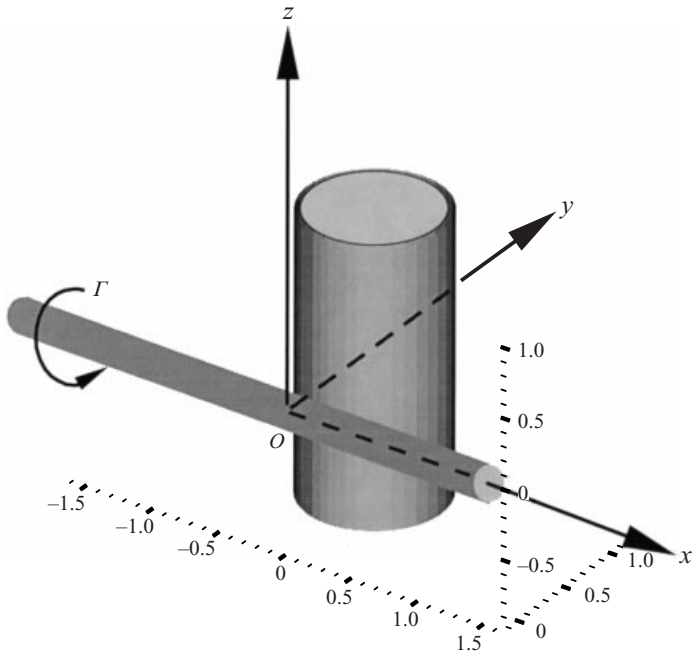

FIGURE 3. Diagram showing initial condition for normal vortex–cylinder interaction problem.

(U_x, U_y, U_z)	$Re = 500$	$Re = 1500$
$(0, 0, 0)$	Case 1	Case 2
$(0, 0, U)$	X	Case 3
$(0, 0, -U)$	X	Case 4
$(0, U, 0)$	X	Case 5

TABLE 1. Summary of vortex Reynolds numbers and free-stream velocities examined.

cylinder used in all computations (except case 5) and the coordinate system are shown in figure 3. All parameters are non-dimensionalized using the cylinder diameter D as a lengthscale and D^2/Γ and ρD^3 as time and mass scales, respectively. The vortex core radius is set to 0.1 for all cases, which corresponds to a thickness parameter of $T = 10$. For a zero free-stream condition, vortex Reynolds numbers of 500 (case 1) and 1500 (case 2) are examined. For the $Re = 1500$ case, three additional free-stream conditions are considered: case 3, flow in the direction of the positive z-axis, such that vorticity within the ambient cylinder boundary-layer is oriented in the negative x-direction (opposite to that within the primary vortex) near the cylinder leading edge; case 4, flow in the direction of the negative z-axis, such that vorticity within the ambient cylinder boundary-layer is oriented in the positive x-direction (the same as that within the primary vortex) near the cylinder leading edge; case 5, free-stream flow in the direction of the positive y-axis, advecting the primary vortex toward the cylinder. The free-stream velocity magnitude ($U = 0.334$) is the same in cases 3–5 and is chosen to yield, for case 5, an impact parameter equal to the high impact parameter case ($I = 0.21$) examined using inviscid computations and flow-visualization experiments by Krishnamoorthy *et al.* (1999).

Although the value of impact parameter considered in the paper is typical of many applications, such as those discussed in § 1, the values of the vortex Reynolds number are much smaller than would ordinarily be found in many of these applications. For instance, estimates of vortex strength and impact parameter for the problem of helicopter main rotor interaction with the tail section (Krishnamoorthy & Marshall 1998) give impact parameters in the range $0.04 < I < 0.9$ and vortex Reynolds numbers of the order of $Re \cong 0.1(VR/\nu)$ as the helicopter advance ratio μ spans the range $0 < \mu < 0.4$ typical of normal flight conditions. Here, V is the helicopter flight speed, R is the rotor radius and ν is the kinematic viscosity. Choosing $V = 50\,\mathrm{m\,s^{-1}}$, $R = 10\,\mathrm{m}$ and $\nu = 1.5 \times 10^{-5}\,\mathrm{m^2\,s^{-1}}$ gives a typical rotor wake vortex Reynolds number of $Re \simeq 3 \times 10^7$. As mentioned in § 1, previous computations using boundary-layer theory by Affes *et al.* (1994) indicate that the normal vortex–cylinder interaction problem is insensitive to variation of Reynolds number over several orders of magnitude.

The primary vortex is represented using an inviscid filament model (Knio & Ghoniem 1990), in which the vortex filament is discretized by overlapping Gaussian blobs whose amplitudes vary in proportion to the local stretch. Inviscid vortex bending in the presence of the cylinder is computed separately, and the velocity induced by the vortex is treated as a prescribed forcing field in the boundary-layer calculation. This approach neglects vortex core shape deformation and bending induced by the ejected secondary vorticity, which are observed in flow-visualization experiments by Krishnamoorthy *et al.* (1999) to be small during the initial stages after boundary-layer separation (as the secondary vorticity wraps approximately once around the primary vortex) for cases similar to those considered in the current paper. The boundary-layer calculations by Affes *et al.* (1994) and Xiao *et al.* (1997) similarly use a vortex filament model to approximate the forcing from the primary vortex. Use of the inviscid filament model for the primary vortex allows the computations for the cylinder boundary layer response and the initial stages of secondary vorticity ejection to be performed with a larger timestep than would otherwise be possible (by a factor of about 5) and it speeds up formation of the tetrahedral mesh.

For cases 1–4, the vortex filament is initialized as a straight line oriented in the x-direction (figure 3), separated by a distance $d = 0.3$ from the cylinder leading edge. The vortex filament is resolved over an axial length of 4 using 160 vortex blobs, and both ends of the computed section of the vortex filament are connected to semi-infinite straight filaments (Dhanak 1981). For case 5, we attempt to account for the experimentally observed bending of the vortex as it is advected toward the cylinder. For this reason, the vortex filament computation is started at an earlier time ($t = -2.64$) in case 5 than the boundary-layer computation ($t = 0$), so that at the start of the boundary-layer computation, the vortex filament already exhibits significant bending. The times for start of the filament and boundary-layer calculations are selected to be well before substantial vortex bending and at a time slightly before boundary-layer separation, respectively, based on the experimental and numerical results of Krishnamoorthy *et al.* (1999). The number of vortex blobs used to discretize the filament in case 5 is increased to 320, twice that used for cases 1–4, in order to resolve greater bending and stretching of the filament. For all cases considered, the cylinder surface is discretized using 2160 triangular source panels connected to 1116 body computation points. The spacing between the body computation points is uniform in the spanwise direction, but adjusted in the azimuthal direction such that the distance between adjacent points near the front of the cylinder is half that in the rear of the cylinder.

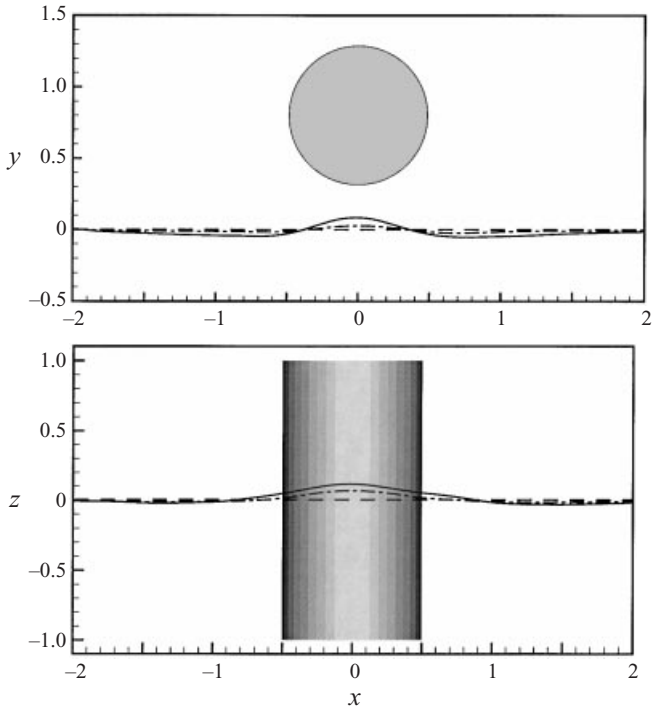

FIGURE 4. Results for bending of vortex filament for case with initial separation distance $d = 0.3$ and no free-stream velocity at times – – –, $t = 0$; – · –, $t = 1$; ——, $t = 2$.

The flow is assumed to be periodic in the spanwise direction. In computing the boundary layer vorticity, two periods of the flow domain and one period of the body source panels on each side of the computed domain are used in the Biot-Savart integral. Test calculations using up to five periods of the vorticity field on each side show no discernable difference from the results with two periods. For the filament computations, three periods of the vorticity field and two periods of the body are used on each side of the computed flow domain.

It is desirable that the period length λ be sufficiently large compared to the relevant lengthscales associated with the secondary vorticity structure so that flow with periodic spanwise boundary conditions is at least qualitatively similar to flow with a single primary vortex impacting an infinitely long cylinder. The most important lengthscale influencing the ejection of secondary vorticity from the cylinder is the vortex–cylinder separation distance, d. The lengthscales associated with the secondary vorticity field after it is ejected from the cylinder surface, such as the loop leg separation distance and the vorticity ejection distance from the body, are also found in the computations to be of $O(d)$. The maximum value of d occurs in the initial configuration, at which time $d/\lambda = 0.15$ for all cases considered.

Vortex filament computations are performed, in order to establish the forcing of the boundary layer by the primary vortex, with the vortex initially oriented parallel to the x-axis and separated from the cylinder leading edge by a distance d. Two cases are considered: (i) $d = 0.3$ and no free-stream velocity, and (ii) $d = 1.5$ and a free-stream velocity of $U = 0.334$ normal to the body. Cases 1–4 in table 1 use filament calculation (i), where the filament is advected along the cylinder axis for cases 3 and 4. Case 5 uses filament calculation (ii). The results for the two filament

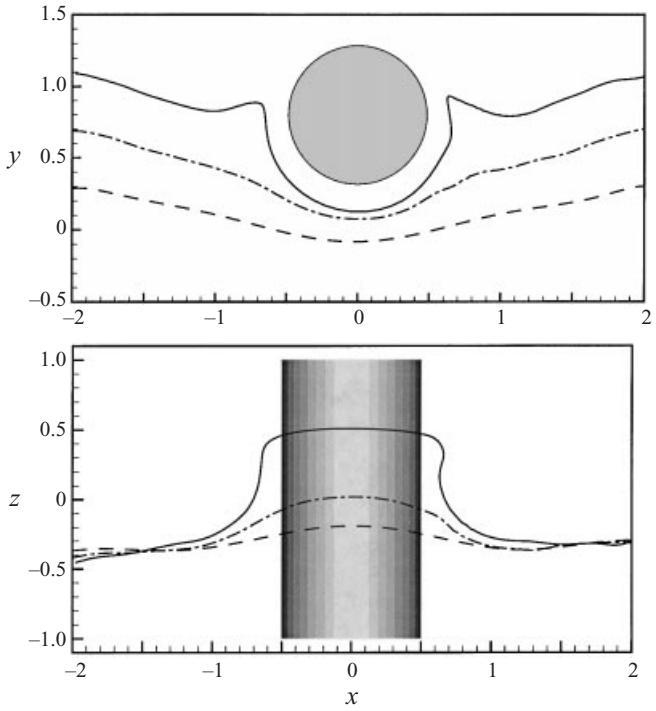

FIGURE 5. Results for bending of vortex filament for case with initial separation distance $d = 1.5$ at $t = -2.64$ and with free-stream velocity $U = 0.334$ normal to the cylinder, shown at times – – –, $t = 0$; – · –, $t = 1$; ——, $t = 2$.

calculations (shown in figures 4 and 5) are typical of the behaviour noted by Marshall & Yalamanchili (1994) for low- and high-impact-parameter cases. In calculation (i), the filament first bends in the cylinder axial direction owing to the velocity induced by its image. The self-induced velocity of the bent vortex then causes it to bend toward the cylinder, giving the appearance that the vortex is attracted to the cylinder. The amplitude of vortex bending is small during the time considered in the cylinder boundary-layer computation. In calculation (ii), the vortex is deflected both in the cylinder axial direction by its image and in the direction opposite to the free-stream velocity owing to the velocity induced by the cylinder in response to the free-stream flow. The latter deflection gives the appearance that the vortex is repulsed from the cylinder. During the time considered in the boundary-layer computation ($0 \leqslant t \leqslant 2$), the vortex wraps around the cylinder and nearly reconnects on the cylinder back face.

The boundary-layer computations are initialized using five fixed 'Euler layers' of staggered computation points, such that the first layer is formed of the body points, the second layer is located at a fixed distance above the panel centroids, the third layer is located above the body points, and so on. The Euler layer points evolve in the same manner as the Lagrangian points, as described in § 2, but are then interpolated back to their initial position at the end of each timestep. The use of an Euler layer of this type is not absolutely necessary for the numerical method described in § 2, since the differentiation and integration algorithms function equally well with regularly and irregularly spaced points, but having such a layer helps to maintain a minimum resolution of the boundary layer all around the body.

Above the Euler layer, the boundary-layer flow is initialized using two staggered layers of Lagrangian computation points, which are advected both by the fluid velocity and by the diffusion velocity. No regridding of the Lagrangian points above the Euler layer is used. A new Lagrangian computation point is added when the distance between the top of the Euler layer and the nearest Lagrangian point above the panel exceeds a specified distance (0.0183). Lagrangian computational points with separation distance less than a specified value (0.0092) are amalgamated by removing both points and creating a new point with vorticity equal to the average of that of the two amalgamated points. In fitting a tetrahedral mesh to the computation points, it is necessary to limit the size of the tetrahedral elements by deleting tetrahedra whose maximum side length exceeds a specified value. In the current computations, the maximum tetrahedral side length is set as 0.3 within the cylinder boundary layer, but is reduced to 0.1 for the ejected vorticity outside of the boundary layer (outside of a radial distance of 1.05 from the cylinder axis). This reduction in value of maximum tetrahedral side length for the ejected vorticity computation points is done to eliminate tetrahedra that might span from points in the ejected vorticity region to points in the cylinder boundary layer. The total number of tetrahedra varied between about 70 000 near the start to about 200 000 near the end of the runs.

The cylinder boundary layer is initialized using an exponential vorticity profile which decays by a factor of e over a distance of 0.055. The strength of this exponential profile is adjusted by an iterative process to enforce the no-slip condition on the body panel centroids at the initial time.

A second-order predictor–corrector method is used to advance the boundary-layer computations in time, with the timestep held fixed at 0.01 for all cases. Between 5 and 15 diffusion substeps are used within each of the larger timesteps to satisfy the stability restriction

$$\frac{2\nu\,\Delta t}{s\ell^2} < 1, \tag{15}$$

where ℓ is a measure of the minimum distance between any two computational points and s is a parameter (called the 'stability parameter') that is found empirically to be about 7–9. In the current computations, the number of diffusion substeps is adjusted adaptively to satisfy (15) with the stability parameter set to unity.

Sensitivity of the computations to selection of timestep and spatial resolution was tested by repeating the first half of the computation for case 1 with a high-resolution run, which used approximately twice as many body source panels (4576) and slightly less than half the timestep (0.004). The high-resolution calculation was terminated at time $t = 0.75$, at which point the boundary layer has separated and secondary vorticity has been pulled outward from the body and has formed a distinct structural form that is beginning to wrap around the primary vortex. It is the first part of the computation, during the initial separation and ejection of vorticity from the body, in which the results are most sensitive to computational resolution. Other computations with fewer computational points indicate that the long-time evolution of the secondary vorticity structure is insensitive to the numerical resolution and to the initialization of the cylinder boundary layer. At the ending time of the high-resolution calculation, the boundary layer is resolved by approximately 250 000 tetrahedra in the high-resolution computation and by 160 000 tetrahedra in the computation reported for case 1. The two computations are qualitatively nearly identical in terms of separation onset and location. Quantitative comparisons between the two runs at the ending time (shown in table 2) indicate differences of only a few per cent in a variety of flow diagnostics.

Quantity	Case 1	High-resolution comparison run	Percentage difference
Maximum vorticity magnitude, $\|\boldsymbol{\omega}\|_{max}$	21.8	22.4	2.7
Cylinder normal force, F_y	−0.0154	−0.0162	4.9
Enstrophy, $E = \frac{1}{2}\int_V \omega^2 \, \mathrm{d}v$	4.5	4.3	4.4
Helicity, $J = \int_V \boldsymbol{u}\cdot\boldsymbol{\omega} \, \mathrm{d}v$	−0.0239	−0.0223	6.7

TABLE 2. Quantitative results at time $t = 0.75$ for case 1 and a high-resolution comparison computation.

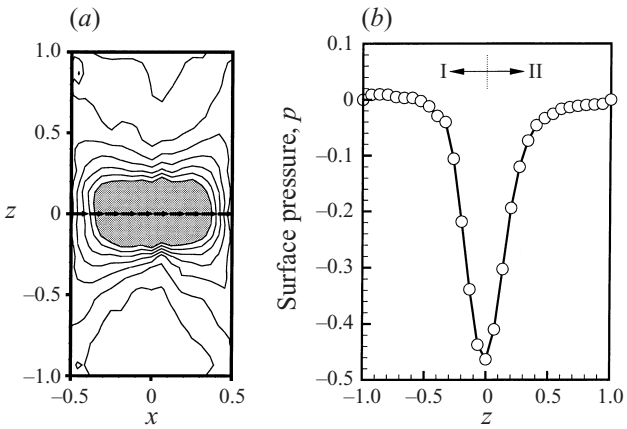

FIGURE 6. Plot of the cylinder pressure field for case 2 at the initial time, showing (*a*) pressure contours on the front of the cylinder and (*b*) pressure variation along the cylinder leading edge. The projection of the vortex filament is indicated by arrows in (*a*), and the contour levels vary in eight even increments from 0.02 to −0.2. Regions with $p < -0.2$ are shaded grey. Regions of (I) favourable and (II) adverse axial pressure gradient are marked in (*b*).

4. Results for impulsive vortex start-up at $Re = 1500$

A vortex filament in the proximity of a cylinder with no free-stream velocity induces a minimum of the pressure field on the cylinder surface directly under the vortex. When the vortex is columnar and oriented normal to the cylinder, as shown in figure 3, and flow is inviscid, the induced pressure field is nearly symmetric on the two sides of the cylinder because of the symmetry in velocity magnitudes. In a viscous flow with a vortex started impulsively at a given position above a cylinder, the surface pressure field is close to that predicted by inviscid theory at the initial time. For instance, a surface pressure contour plot is shown in figure 6(*a*) for the viscous flow computation in case 2 (see table 1) at the initial time, which shows approximate symmetry of the pressure field on the two sides of the vortex filament (indicated by arrows). Since the direction of the velocity induced by the vortex near the surface has everywhere a positive z-component, it is clear that the axial pressure gradient within the cylinder boundary layer is favourable in the region $z < 0$ and adverse in the region $z > 0$. The two regions of (I) favourable and (II) adverse axial pressure gradient are indicated in a plot of the pressure along the cylinder leading edge versus axial distance in figure 6(*b*).

The cylinder boundary layer responds to the vortex-induced pressure field by formation of backflow in the axial direction within the adverse pressure gradient

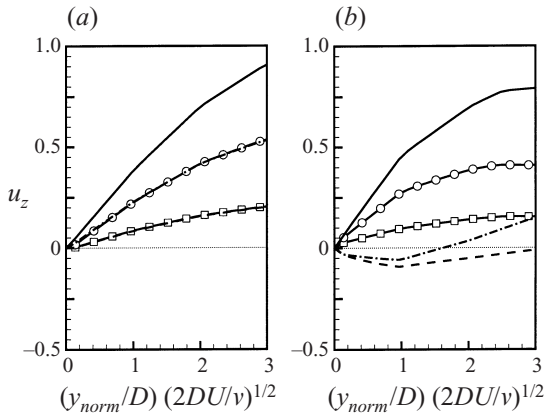

FIGURE 7. Profiles of axial velocity within the cylinder boundary layer as a function of the normal distance, $y_{norm} \equiv 0.3 - y$, at five positions along the cylinder leading edge for case 2 at times (*a*) $t = 0$; (*b*) $t = 0.6$. The profiles are located at □, $z = -0.4$; ○, $z = -0.2$; ——, $z = 0$; –·–, $z = 0.2$; – – –, $z = 0.4$.

region, followed by development of a separation line on the body and ejection of boundary-layer vorticity into the flow. In various test computations with different initial conditions, the time to separation is observed to be sensitive to the initial vorticity profile in the boundary layer, although the qualitative behaviour and the characteristics of the ejected vorticity are the same. This observation may account for the differences in computational predictions of separation onset and experimental observations reported by Affes *et al.* (1998). Boundary-layer velocity profiles at five locations along the cylinder leading edge at the initial time and at a time following separation are shown in figure 7 for the initial condition reported in § 3. At the initial time, the velocity magnitude profiles in the boundary layer are symmetric about the vortex axis. This symmetry quickly breaks down as surface vorticity magnitude along the leading edge decreases in the adverse pressure gradient region above the vortex, and increases in the favourable pressure gradient region below the vortex. Flow reversal along the cylinder leading edge is first observed to occur just before time $t = 0.2$, and the flow reversal region grows larger and the reverse velocity magnitude increases with time.

Plots of surface limiting streamlines and vortex lines over the half of the cylinder facing the vortex are given in figures 8 and 9 at three times. The limiting streamlines are obtained using the velocity at the first computational point above the surface within the Euler layer. Both streamlines and vortex lines are symmetric about the plane $z = 0$ at the initial time. A node in the limiting streamlines becomes apparent just above the vortex filament at time $t = 0.2$, with a saddle point just above the node. In the time interval $0.2 \leqslant t \leqslant 0.6$, the stable node remains fixed but the saddle moves upward until the node receives backflowing fluid from the entire cylinder surface above the node. The total number of nodes on the cylinder is at all times equal to the number of saddle points, as required by the topological constraint for flows with bodies having periodic end conditions (Tobak & Peake 1982). A focus point forms in the vortex lines at time $t = 0.6$ at the same position as the node in the limiting streamlines. Starting with time approximately $t = 0.8$, the node in the streamlines bifurcates into stable nodes joined by a line of separation, with a saddle point at the midpoint of the separation line. The two nodes gradually move apart with time. The

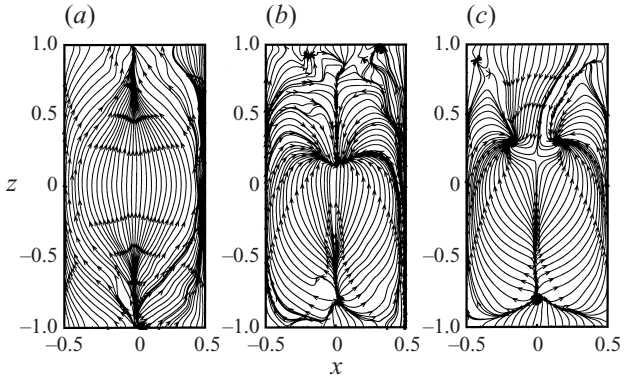

FIGURE 8. Limiting streamlines on the cylinder surface for case 2 at times (*a*) $t = 0$; (*b*) $t = 0.6$; (*c*) $t = 1.4$.

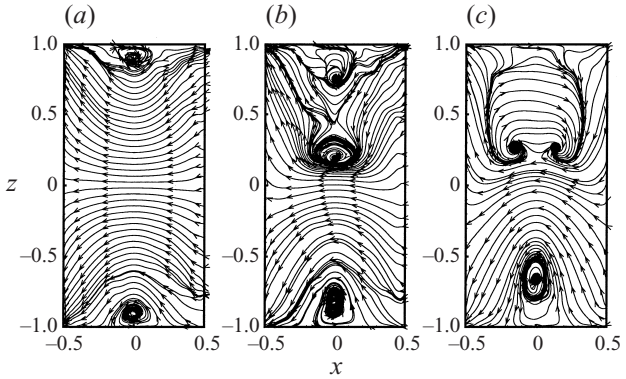

FIGURE 9. Vortex lines on the cylinder surface for case 2 at times (*a*) $t = 0$; (*b*) $t = 0.6$; (*c*) $t = 1.4$.

focus in the surface vortex lines similarly bifurcates into two foci with rotation of opposite sign, located at the same positions as the nodes in the limiting streamlines. The observed topological structure of the limiting surface streamlines and vortex lines in the vicinity of the vorticity ejection location is in agreement with that observed in the computations of Affes *et al.* (1994) using the boundary-layer equations and is similar to the pattern referred to as an 'owl face of the second kind' by Perry & Chong (1987), who analysed this structure using critical-point theory.

A contour plot of the vorticity magnitude on the cylinder surface at time $t = 1.2$ is given in figure 10, on which is superposed indicators of major topological features of the surface limiting streamlines. A saddle point is denoted by X and a nodal point is denoted by a circle with N above it. The separation curve is indicated by a heavy solid line. A region of high vorticity magnitude is located directly below the vortex filament, corresponding to vorticity oriented primarily in the negative x-direction (opposite in sign to that within the vortex filament) generated because of the strong velocity in the z-direction induced by the vortex filament. We recall that the vortex lines within the secondary loop must fan outward into the cylinder boundary layer near the points of loop attachment to the body, in order to satisfy the condition $\boldsymbol{\omega} \cdot \boldsymbol{n} = 0$ at the surface. Since the swirling velocity is low within the inner part of the secondary vortex loop

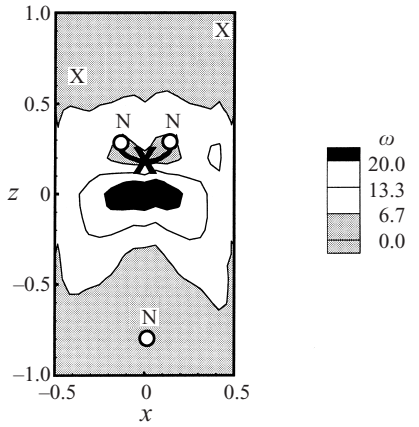

FIGURE 10. Vorticity magnitude contours on the cylinder surface at time $t = 1.4$ for case 2. Surface topological features are indicated using N for a node (with a circle marking the node position), X for a saddle, and a bold curve for the separation line connecting two nodes.

core, the two nodes corresponding to loop attachment points are located in regions of low vorticity magnitude.

Evolution of the ejected secondary vorticity support over time can be observed in figure 11, which shows velocity vectors attached to Lagrangian computational points in a thin slice of the computed flow, in the range $-0.2 \leqslant x \leqslant 0.2$. At time $t = 0.6$, the boundary layer exhibits a pronounced bulge centred at a point above the cylinder surface at about a 45° angle from the primary vortex filament. At later time, the secondary vorticity is drawn outward from the cylinder boundary and wraps around the primary vortex. The minimum separation distance between the primary vortex and the secondary vorticity structure decreases gradually as the fluid is advected around the vortex. Radial entrainment of the ejected vorticity into the primary vortex is also observed in figure 11, which is caused by the self-induced velocity of the secondary vorticity structure.

A contour plot of the y-component of vorticity, ω_y, and corresponding streamlines in an (x, z)-planar slice at $y = 0.2$, near the base of the secondary vorticity structure, are plotted in figure 12 at time $t = 1.4$. The vorticity field has the form of a pair of counter-rotating vortices centred directly above the nodal points in the streamline plots, which correspond to cross-sections of the secondary vorticity loop. These counter-rotating vortices strengthen and move farther apart with time. The sign of the vorticity within these cross-sections in figure 12 indicates that the self-induced velocity of the secondary vorticity structure is oriented radially inward toward the primary vortex, which is consistent with the observed radial entrainment of the Lagrangian points. A three-dimensional view of the iso-surface with vorticity magnitude $\omega = 5$ is shown in figure 13 in an orthographic view in the (x, z)-plane. The form of the secondary vorticity structure observed in the computations is similar to that described by Krishnamoorthy *et al.* (1999) for low-impact-parameter cases based on flow visualization experiments.

An important issue in evaluating the limitations of inviscid computational methods for vortex–body interaction, such as commonly used in rotorcraft design, involves the significance of the ejected secondary vorticity on the surface pressure field and net force on the body. To examine this issue, the surface pressure field on the cylinder surface for both inviscid and viscous flow cases is plotted in figure 14 at time $t = 1.4$,

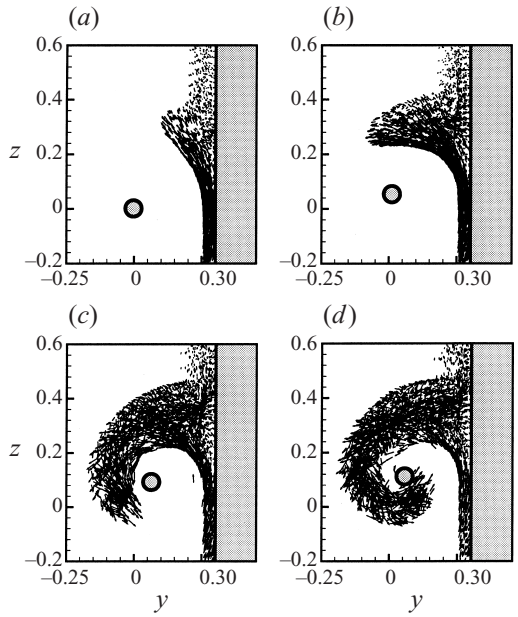

FIGURE 11. Velocity vectors attached to the Lagrangian computational points in a thin slice centred on the (y,z)-plane $(-0.2 \leqslant x \leqslant 0.2)$ at times (*a*) $t = 0.6$; (*b*) $t = 1.0$; (*c*) $t = 1.4$; (*d*) $t = 1.6$. The cross-section of the primary vortex is indicated by a grey-filled circle.

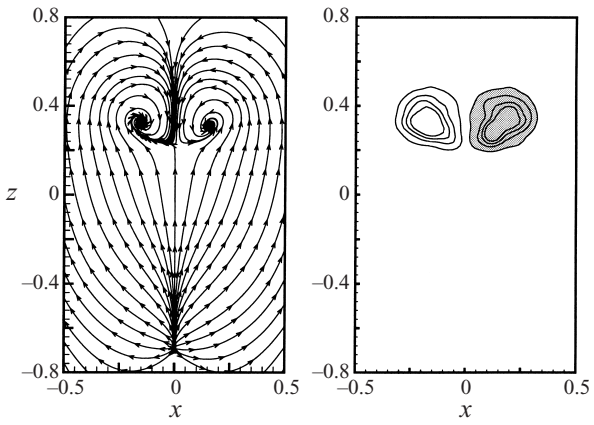

FIGURE 12. Streamlines and contours of ω_y over a planar slice of the flow at $y = 0.2$, near the base of the ejected vorticity structure, for case 2 at time $t = 1.4$. Regions with $\omega_y < -1.1$ are shaded grey.

at which point the secondary vorticity loop has wrapped approximately three-quarters of the way around the primary vortex. The pressure contours in the inviscid-flow case remain roughly symmetric on the two sides of the vortex filament, with a region of minimum pressure located directly below the vortex filament. The pressure field is quite different in the viscous-flow case. The low-pressure region moves upward into a U-shaped region above the vortex filament, and a high-pressure region forms just below the vortex filament near the centre of the cylinder face. Moreover, the region

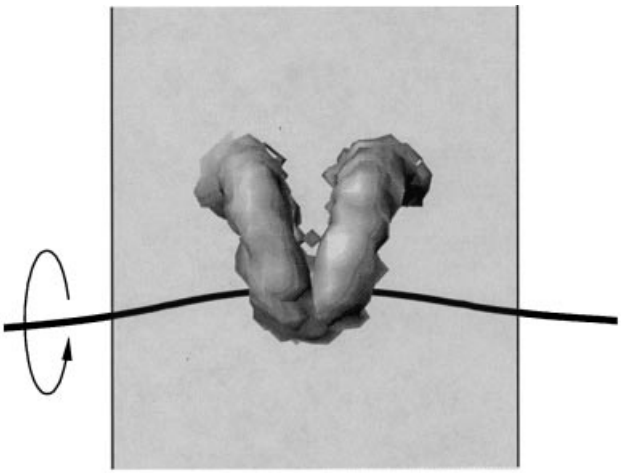

FIGURE 13. Orthographic view in the (x, z)-plane of an iso-surface of vorticity magnitude ($\omega = 5$) for case 2 at time $t = 1.4$, showing the loop-like form of the ejected secondary vorticity structure. The cylinder surface is indicated by light grey shading and the primary vortex position is indicated by a solid black line.

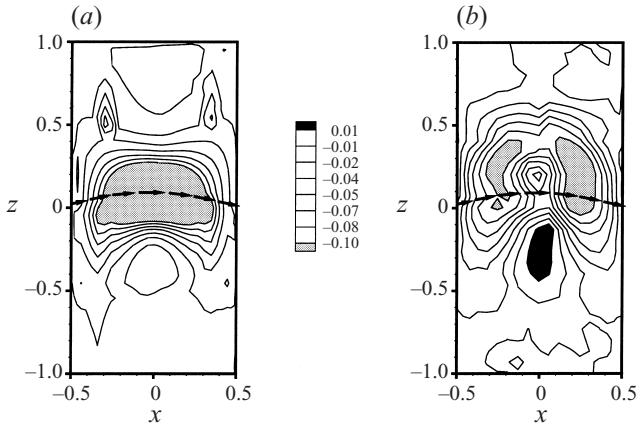

FIGURE 14. Pressure contours on the cylinder surface for case 2 at time $t = 1.4$ for (*a*) inviscid and (*b*) viscous flow calculations. The projection of the vortex filament is indicated by arrows.

of lowest pressure bifurcates and moves to positions on the cylinder surface below which the secondary vortex loops attach to the cylinder boundary layer.

The streamlines in the (y, z)-plane at $x = 0$, bisecting the cylinder directly between the two legs of the secondary vortex loop, are shown in figure 15 at the initial time and at time $t = 1.2$. At the initial time, the boundary layer is attached and the secondary vorticity has essentially no effect on the flow field external to the boundary layer. The external velocity field is observed to be symmetric about the vortex filament location and to have a positive axial component of velocity close to the cylinder. At time $t = 1.2$, the secondary vorticity has wrapped over half-way around the primary vortex. The symmetry of the external flow field is broken and a downward reverse flow is observed in the region above the primary vortex. A dividing streamline between the positive and negative axial velocity regions projects out of the body at approximately the location of the saddle point in the surface streamlines shown in figure 10.

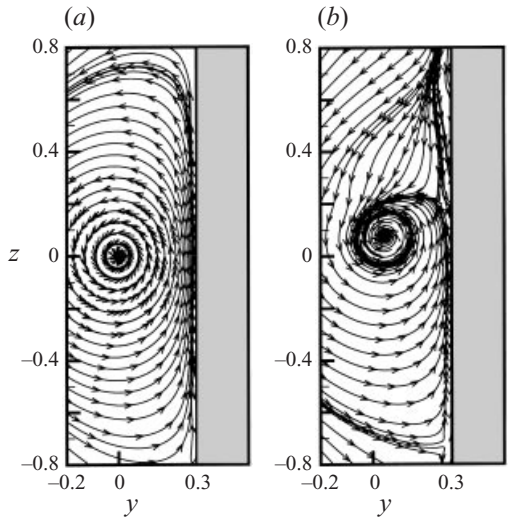

FIGURE 15. Streamlines in the (y, z)-plane at $x = 0$ (the plane bisecting the two legs of the secondary vortex loop) for case 2 at times (*a*) $t = 0$, and (*b*) $t = 1.2$, showing the effect of the ejected secondary vorticity on the velocity field external to the boundary layer.

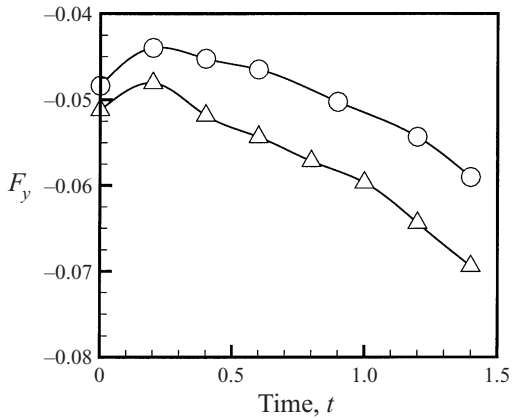

FIGURE 16. Time variation of the total force component normal to the cylinder axis (y-direction) for △, inviscid flow, and ○, viscous flow.

The net force acting normal to the cylinder (in the y-direction) is plotted for both inviscid- and viscous-flow cases in figure 16. For viscous flow, only about 2–5% of the total force is due to shear at the boundary. In contrast to the pressure field, the net force exhibits only moderate differences between the viscous- and inviscid-flow computations for the case with no free-stream velocity, with the force magnitude for inviscid flow about 20% higher than that for viscous flow. The most significant effect of the secondary vorticity on the net cylinder force for this case may occur not through its direct action on the pressure force, but rather indirectly through interaction of the secondary vorticity with the primary vortex. This interaction was precluded from consideration in the present study by use of the filament theory approximation for the primary vortex, but it has been shown in previous work using both experimental and computational methods (Melander & Hussain 1993; Marshall 1997; Krishnamoorthy

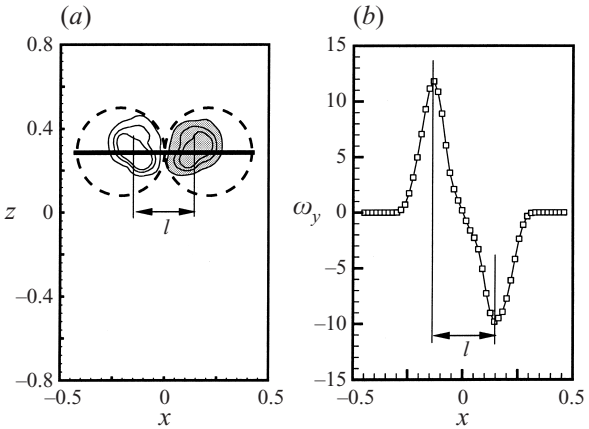

FIGURE 17. Contour plot of ω_y in the plane $y = 0.2$ at time $t = 1.0$ for case 2, showing – – –, contours used for calculation of circulation Γ_s and the definition of the vortex loop separation distance l. Regions with $\omega_y \leqslant -1.0$ are shaded grey. Variation of vorticity versus distance on the line drawn in (*a*) is plotted in (*b*), showing two peaks of vorticity with ω_y of opposite sign.

& Marshall 1998; Krishnamoorthy *et al.* 1999) that the velocity field induced by the secondary vorticity structures can lead to bending, core shape deformation, and axial wave formation on the primary vortex over a long time interval. If the secondary vorticity is sufficiently strong, it is observed to eventually cause vorticity stripping from the primary vortex, which in some cases is followed by vortex breakdown. The pressure does not vary linearly with the free-stream velocity field, and, in other cases examined, the secondary vorticity has been observed to have significant direct effect on the net cylinder force (Gossler 1999). Also, even when the direct effect of the secondary vorticity on the cylinder force is small, modelling of its interaction with the primary vortex requires knowledge of the structural form that the secondary vorticity develops following ejection from the body.

5. Effect of Reynolds number on ejected vorticity

Parameters that characterize the secondary vorticity loop, including vortex loop strength, maximum vorticity magnitude, and minimum separation distance between locations of peak vorticity (loop legs), are examined in the current section for impulsive vortex start-up with vortex Reynolds numbers of 500 and 1500 (cases 1 and 2). An example showing how these different quantities are calculated is illustrated in figure 17. Figure 17(*a*) shows a contour plot of ω_y in the plane $y = 0.2$ near the base of the secondary vorticity structure. The vorticity contours are dominated by a vortex pair with ω_y of opposite sign. The cores of both vortices, which make up the legs of the secondary vortex loop, are deformed in a manner characteristic of a pair of opposite-sign vortices in two dimensions. The strengths of both the negative and positive sign vortices in this cross-section are calculated using the contours indicated by dashed lines in figure 17(*a*), both by integrating ω_y over the area enclosed by the contour and by integrating the tangential component of velocity around the contour. The vorticity values are extracted on a line passing through the peak values of ω_y in the two vortex patches, as shown in figure 17(*b*), and the parameter l denotes the distance between the peak vorticity locations.

Data for strength of the secondary vortices in the plane $y = 0.2$ as a function

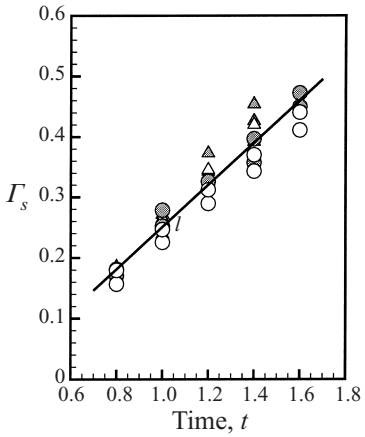

FIGURE 18. Data for time variation for the secondary vortex strength measured in the plane $y = 0.2$ near the base of the vortex structure. Filled symbols denote data computed using area integration of vorticity, while open symbols denote data computed using integration of velocity about the contour. ▲ △, $Re = 500$; ● ○, $Re = 1500$; ——, best fit to the data.

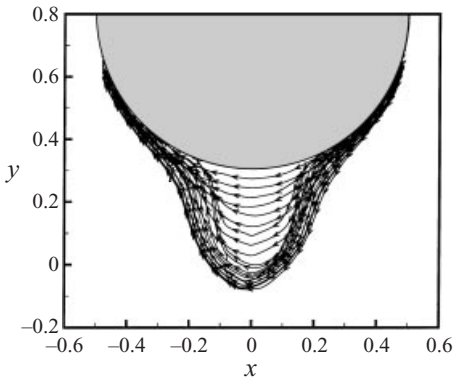

FIGURE 19. Vortex lines in the ejected vorticity structure for case 2 at time $t = 1.0$, showing spanning of vortex lines between the two strong legs of the vortex loop.

of time is given in figure 18. Open symbols denote values calculated using contour integration of tangential velocity, and filled symbols denote values calculated using area integration of ω_y. The root-mean-square difference between vortex strength values obtained using these two methods is 0.036, or about 10%. Circles denote data for $Re = 1500$ and triangles denote data for $Re = 500$. The computations with different Reynolds numbers yield nearly identical values of vortex strength, which is a consequence of the fact that the boundary-layer strength is determined from the external inviscid flow and the location of boundary-layer separation is not sensitive to Reynolds number.

The data in figure 18 indicate that the secondary vortex strength increases nearly linearly with time when measured at a fixed location. This trend is not consistent with what we would expect for a simple hairpin vortex surrounded by irrotational fluid, for which the strength must be uniform along the vortex tube. To explain the observed increase with time of the secondary vortex strength, a plot of vortex lines within the secondary vortex structure is given in figure 19 for case 2 at time $t = 1.0$.

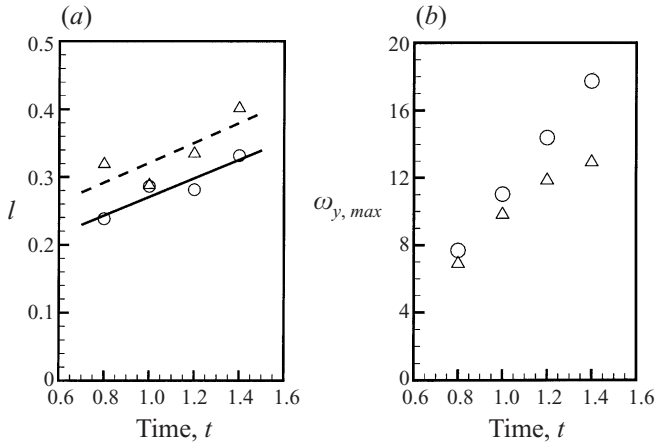

FIGURE 20. Data for time variation of (*a*) vortex loop separation distance l, and (*b*) maximum vorticity magnitude in a cross-section of the secondary vorticity structure at $y = 0.2$. ○, ——, data for $Re = 1500$; △, – – –, data for $Re = 500$.

These vortex lines originate in the cylinder boundary layer, arch outward into the ejected vortex structure, and then rejoin the cylinder boundary layer on the other side. A high concentration of vortex lines around the periphery of the ejected vorticity field marks the strong loop-like vortex that forms from roll up of the secondary vorticity tongue as it is ejected outward. In between the legs of this vortex loop lies a vorticity sheet, across which vortex lines span to connect the loop legs. Because of the presence of this vorticity sheet, the legs of the loop-like vortex structure do not form a vortex tube, and the strength is consequently not restricted to be uniform along the length of these legs.

Data for vortex leg separation distance l and maximum ω_y magnitude are given in the plane $y = 0.2$ in figure 20 for both $Re = 500$ and $Re = 1500$. The value of l is similar in both cases, but is found to be about 12% higher in the $Re = 500$ case than in the $Re = 1500$ case. The maximum vorticity is initially very similar in both cases, which is due to the fact that the boundary-layer vorticity is initialized in the same way for both computations. Over time, the vorticity in the $Re = 500$ case becomes less than that in the $Re = 1500$ case by up to 25%.

The data in figures 18 and 20 are given for a single cross-sectional plane of the secondary vortex structure. Kelvin's theorem requires that the strength of a material circuit is invariant if the vorticity flux vanishes on the circuit about which the circulation is computed. This theorem suggests that the vortex strength should be 'frozen in' to the secondary vortex structure, provided that cross-diffusion of vorticity between the two vortex legs can be neglected. To test this idea, data for vortex strength are measured over a series of (x, z)-slices at different values of the normal distance, $y_{norm} \equiv 0.3 - y$, from the cylinder leading edge. It is observed that the velocity V_n of the tip of the secondary vorticity structure is approximately constant over the time interval $0.6 \leqslant t \leqslant 1.0$, during which the secondary vorticity is pulled away from the cylinder boundary layer and just begins to wrap around the primary vortex. Dividing the distance between the measuring plane and the plane $y = 0.2$ used in figure 18 by V_n yields the difference between the time at which the measurement is taken and the effective time at which the material circuit was located in the plane $y = 0.2$. The value of the vortex strength given by the mean line at this effective time in figure 18 is

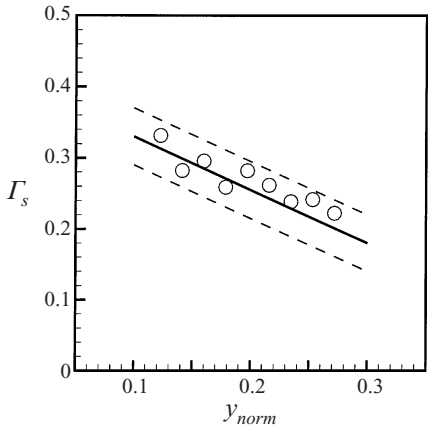

FIGURE 21. Secondary vortex strength as a function of distance normal to the cylinder leading edge for case 2 at time $t = 1.2$. ○, measured data; ——, predicted values from the best-fit line of figure 18, assuming frozen vorticity field; – – –, the uncertainty band of the prediction, owing to scatter in figure 18.

compared to the measured vortex strength data in figure 21. Two dashed lines drawn parallel to the mean line indicate uncertainty in the predicted Γ_s owing to data scatter in figure 18. The measured data in figure 21 are all within the uncertainty band of the predicted values.

6. Results with positive and negative axial free-stream velocity

In this section, we examine the effect of free-stream flow in the positive and negative z-directions, parallel to the cylinder axis, on the impulsive vortex start-up case discussed in the previous two sections. The magnitude of the free-stream velocity (0.334) is slightly less than half the maximum slip velocity (0.92) on the cylinder outer boundary layer induced by the vortex. The free-stream velocity gives rise to an ambient azimuthal vorticity field on the cylinder surface. The ambient vorticity increases the boundary-layer vorticity generated by the vortex in case 3 and decreases the boundary-layer vorticity generated by the vortex in case 4. The positive (negative) free-stream velocity advects the vortex toward (away from) the region of adverse axial pressure gradient. It is observed that the vorticity ejection process and the structure of the ejected vorticity field is qualitatively the same in cases with positive and negative axial flow to that with no free-stream velocity. However, vorticity is observed to be ejected at an earlier time in the case with positive axial flow, and at a later time in the case with negative axial flow, than in the case with no free-stream velocity. For instance, the positions of the Lagrangian computational points in a thin slice of the flow field (spanning from $-0.2 \leqslant x \leqslant 0.2$) are shown at time $t = 1.4$ for cases 2–4 in figure 22. For the case with positive free-stream axial velocity, the computational points have wrapped about 75% of the way around the primary vortex, whereas, at the same time, the points have wrapped only about 50% around the primary vortex for the negative free-stream velocity case.

The limiting streamlines and vortex lines on the cylinder surface are shown in figures 23 and 24, where results for positive and negative axial free-stream velocity are shown in parts (*a*) and (*b*), respectively, of each figure. As in the case with no free-stream flow, the ejected vorticity region is characterized by a node that bifurcates

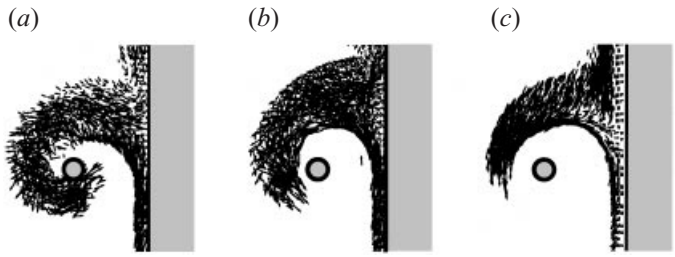

FIGURE 22. Velocity vectors attached to the Lagrangian computational points in a thin slice of the flow ($-0.2 \leqslant x \leqslant 0.2$) at $t = 1.4$ for (*a*) case 3, (*b*) case 2, (*c*) case 4. The cross-section of the primary vortex is indicated by a grey-filled circle.

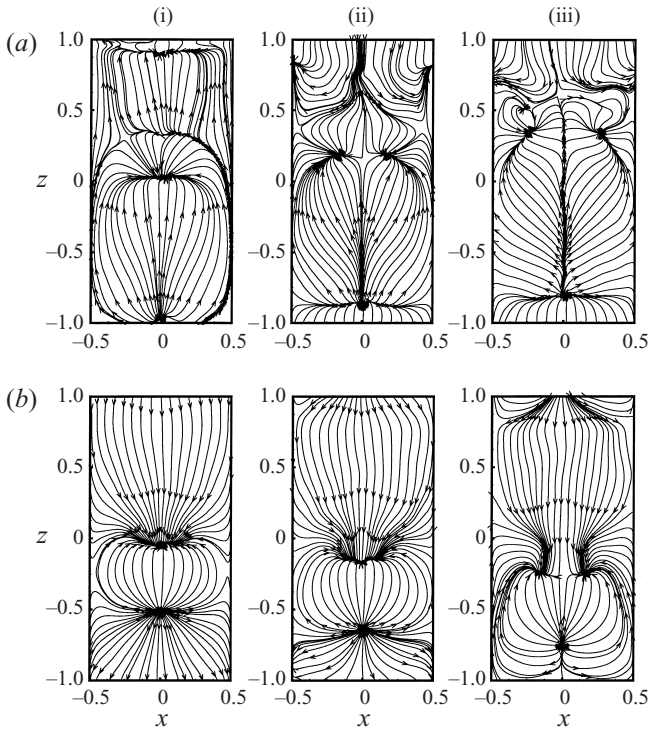

FIGURE 23. Limiting streamlines on the cylinder surface at times (i) $t = 0.6$, (ii) $t = 1.0$, (iii) $t = 1.4$ for (*a*) positive (case 3), (*b*) negative (case 4) free-stream velocity.

into two nodes and a saddle in the limiting streamlines. The vortex lines appear quite different in cases 3 and 4 because the ambient boundary-layer vorticity has opposite sign.

The strength of the ejected secondary vorticity loop, determined by area integration of ω_y in the plane $y = 0.2$, is plotted as a function of time in figure 25 for cases 2–4. In the case with positive axial free-stream velocity, the ambient vorticity adds to that generated by the vortex, and the ejected vortex structure correspondingly has greater strength than for the case with no free-stream velocity. Similarly, in the case with negative free-stream velocity the ambient vorticity detracts from that generated by the vortex and the resulting secondary vortex strength is reduced.

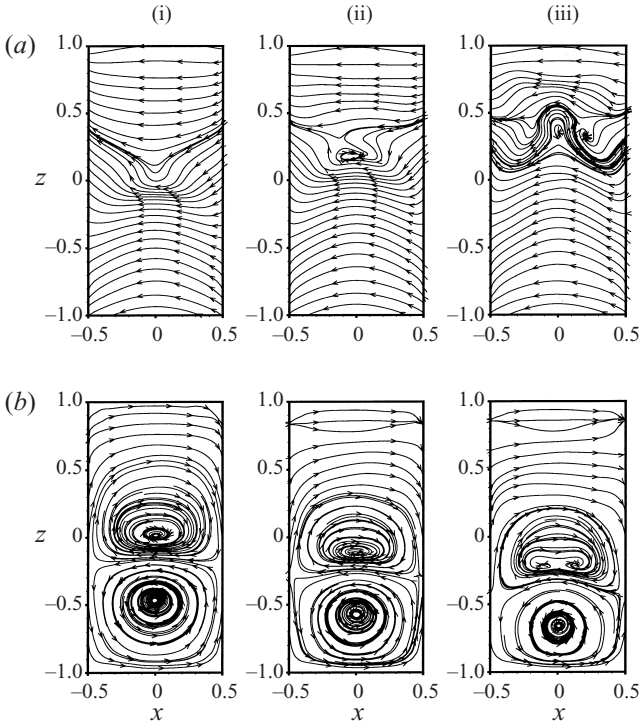

FIGURE 24. Vortex lines on the cylinder surface at times (i) $t = 0.6$, (ii) $t = 1.0$, (iii) $t = 1.4$ for (*a*) positive (case 3), (*b*) negative (case 4) free-stream velocity.

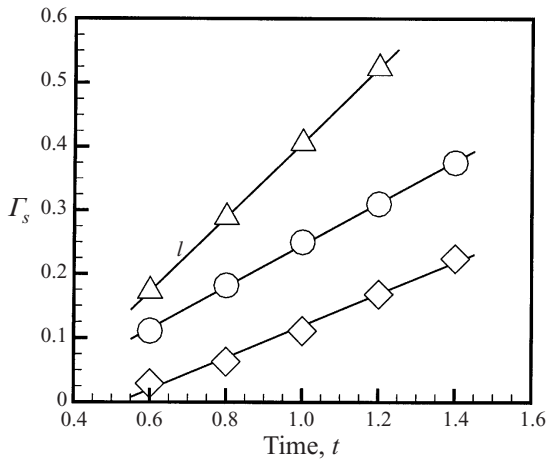

FIGURE 25. Effect of axial free-stream velocity on the strength of the secondary vortex, measured at $y = 0.2$ for △, positive free-stream velocity; ○, no free-stream velocity (case 2); ◇, negative free-stream velocity (case 4).

7. Results with normal free-stream velocity

Most vortex–cylinder interaction problems involve some component of flow directed normal to the cylinder axis, which is responsible for advecting the vortex into the vicinity of the cylinder. The effect of the normal velocity is characterized by the

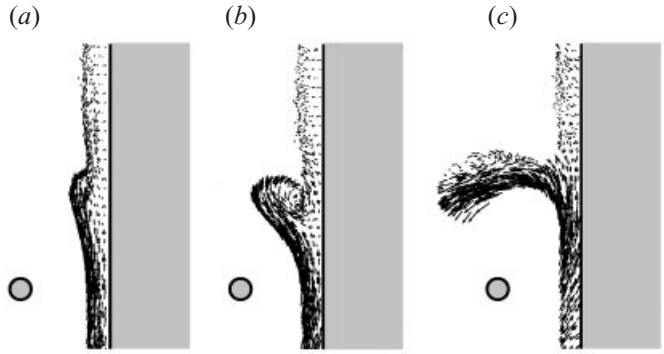

FIGURE 26. Velocity vectors attached to the Lagrangian computational points in a thin slice of the flow field ($-0.2 \leqslant x \leqslant 0.2$) for case 5 at times (*a*) $t = 0.6$, (*b*) $t = 1.0$, (*c*) $t = 14$. The cross-section of the primary vortex is indicated by a grey-filled circle.

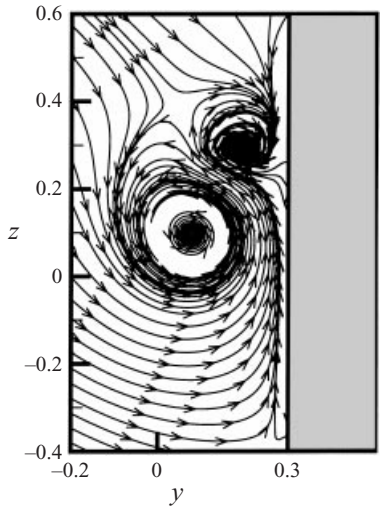

FIGURE 27. Streamlines in a cross-section in the $x = 0$ plane for case 5 at time $t = 1.2$, showing the counter-rotating primary and secondary vortices.

impact parameter $I \equiv 2\pi\sigma U/\Gamma$. Experimental results of Krishnamoorthy *et al.* (1999) indicate that the structure of the secondary vorticity field is very different for flows with high and low values of the impact parameter, as discussed in § 1. The computation performed in case 5 has the same value of impact parameter as the high-impact-parameter case considered by Krishnamoorthy *et al.* (1999). The computational results indicate that the ejected vorticity structure is qualitatively different for this case than for the cases discussed in the previous sections, and the overall form of the ejected vorticity field corresponds roughly to the schematic shown in figure 1(*b*) based on the flow-visualization results of Krishnamoorthy *et al.* (1999).

Positions of the Lagrangian computational points in a thin slice of the flow, in the range $-0.2 \leqslant x \leqslant 0.2$, are shown in figure 26 at three times, along with the cross-section of the primary vortex. The boundary layer gradually thickens in the region above the vortex (figure 26*a*) and forms a secondary vortex structure rotating in the opposite direction to the primary vortex. Unlike the previous cases examined, for this case the secondary vortex remains in the vicinity of the cylinder surface and

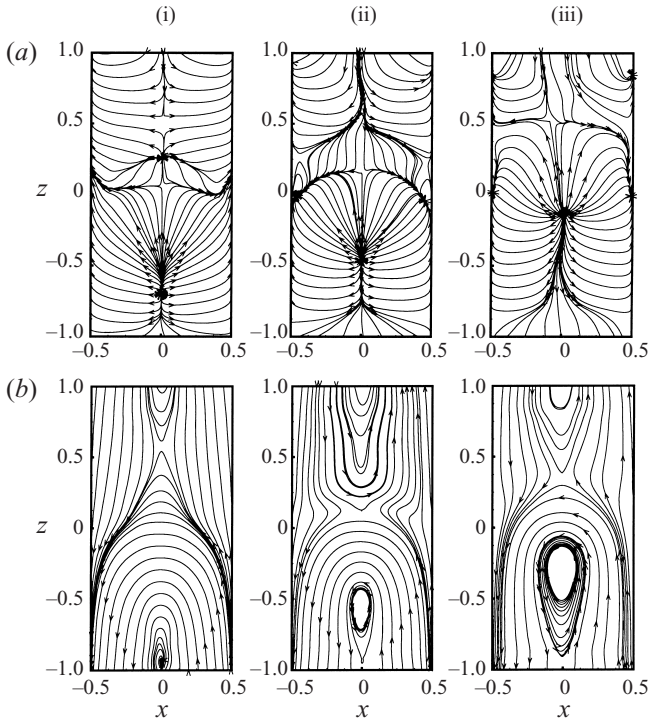

FIGURE 28. Topology of near-surface flow for case 5, showing (*a*) limiting streamlines and (*b*) vortex lines on the cylinder surface at times (i) $t = 0.6$, (ii) $t = 1.0$, (iii) $t = 1.4$.

gradually strengthens for a considerable time after it is formed (figure 26*b*). The secondary vortex is eventually ejected away from the cylinder surface (figure 26*c*) and wraps around the primary vortex. Streamlines in a cross-section at $x = 0$, projecting out of the leading edge of the cylinder, are shown in figure 27. Both the primary and secondary vortices are clearly evident in this cross-section, with a stagnation point on the cylinder surface between the two structures.

A time series of limiting streamlines and vortex lines on the side of the cylinder surface facing the vortex are shown in figures 28(*a*) and 28(*b*), respectively. A separation line in the limiting streamlines occurs between the primary and secondary vortices with a saddle point at the centre. Whereas in cases 1–4 the region of vorticity ejection is characterized by a pair of nodes at the points where the secondary loop vortices attach to the blade boundary layer, surface streamline topology in case 5 is characterized instead by a curved separation line that spans completely around the cylinder front face. The pair of nodal points in the limiting streamlines and foci in the surface vortex lines, which mark the position of vortex loop attachment to the cylinder in cases 1–4, are not observed in case 5.

A plot of an iso-surface of vorticity magnitude ($\omega = 6$) at time $t = 1.2$ is shown in figure 29 in an orthographic view in the (x, z)-plane. The secondary vortex has the form of a ridge of vorticity that wraps around the entire front side of the cylinder. Cross-sections of the azimuthal component of vorticity at different angles around the cylinder are shown in figure 30. The azimuthal vorticity within the secondary vortex has nearly the same strength and core radius over an angle of $\pm 45^\circ$ from the plane $x = 0$ at the cylinder leading edge. The secondary vortex strength gradually decays

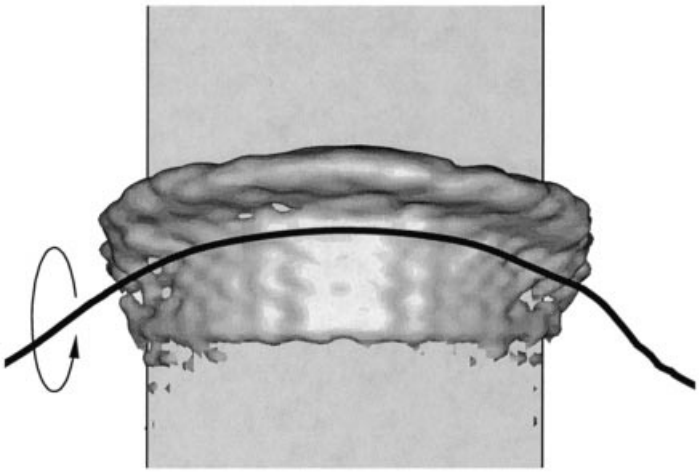

FIGURE 29. Orthographic view in the (x, y)-plane of an iso-surface of vorticity magnitude ($\omega = 6$) for case 5 at time $t = 1.2$, showing a ridge of secondary vorticity oriented mainly in the azimuthal direction and wrapped around the cylinder front surface.

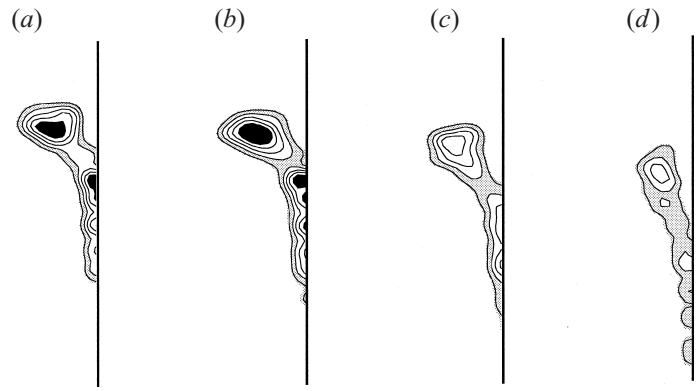

FIGURE 30. Contour plots of the azimuthal component of vorticity for a series of cross-sections through the secondary vortex structure at different angles around the cylinder centre. Plots are given for case 5 at time $t = 1.2$, with angles of (*a*) $\theta = 0°$ (parallel to the free-stream velocity), (*b*) $\theta = 22.5°$, (*c*) $\theta = 45°$, (*d*) $\theta = 67.5°$. Regions with $\omega_\theta \leqslant -15$ are shaded black and regions with $\omega_\theta > -4.6$ are shaded grey.

for angles greater than about 45°. While the secondary vortex is fed from vorticity generated in the boundary layer directly beneath the primary vortex, there exists at all angles a distinguishable region of high azimuthal vorticity that is separate from the boundary-layer vorticity.

In order to examine in more detail the structure of the ejected secondary vorticity, contour plots of ω_x in the plane $x = 0$ and of ω_y in the plane $y = 0.14$ are shown in figure 31 at time $t = 1.4$. The vorticity is found to be oriented principally in the azimuthal direction, such that a large vortex patch is observed in the ω_x contours in the plane projecting out of the cylinder leading edge in figure 31(*a*). Two elongated regions with ω_y of opposite sign are observed in figure 31(*b*), corresponding to locations where the $y = 0.14$ plane slices through the secondary vortex structure as it wraps around the cylinder surface. The circulation of the secondary vortex is

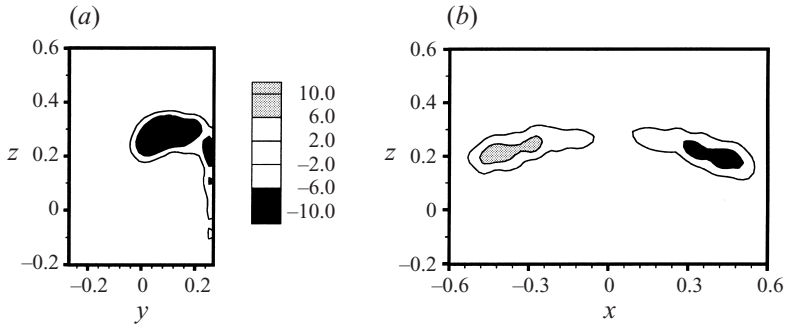

FIGURE 31. Contour plots of (*a*) ω_x in the plane $x = 0$ and (*b*) ω_y in the plane $y = 0.14$ for case 5 at time $t = 1.4$.

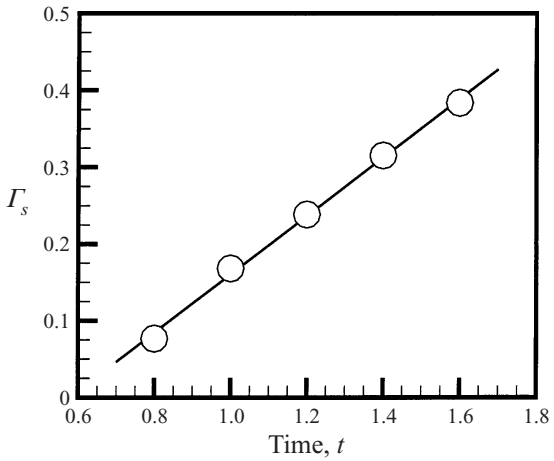

FIGURE 32. Time variation of the strength of secondary vortex structure for case 5, measured in the plane $x = 0$.

computed by area integration of ω_x over a contour in the $x = 0$ plane that surrounds the secondary vortex, but does not include the boundary-layer vorticity. Repeated calculations of circulation with different contours yield only a slight (about 1%) change in vortex strength. The secondary vortex circulation is found to increase nearly linearly in time, as shown in figure 32.

Surface pressure contours for both inviscid and viscous flow at time $t = 1.4$ are shown in figure 33. In the case of free-stream velocity normal to the cylinder, the combination of the vortex-induced velocity and the free-stream velocity causes formation of a positive pressure patch in the stagnation region below the vortex. A high-pressure region in a similar location is present in the inviscid computation results of Affes & Conlisk (1993).

8. Conclusions

The secondary vorticity field generated by a cylinder during interaction with a normal vortex filament is examined under several different free-stream flow conditions. Both for the case of no free-stream velocity and for that with free-stream velocity oriented tangent to the cylinder axis, the secondary vorticity is observed to form a

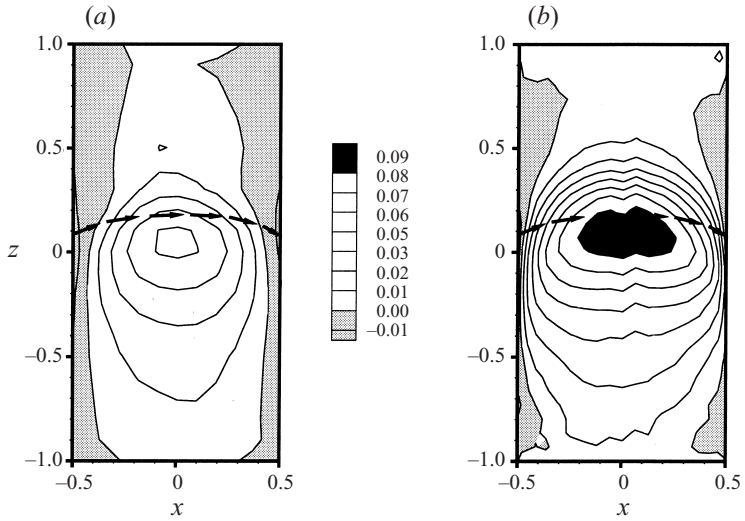

FIGURE 33. Surface pressure contours for case 5 at time $t = 1.4$ for (*a*) inviscid and (*b*) viscous flow. The projection of the vortex filament is indicated by arrows.

loop-like structure that ejects outward from the cylinder surface and wraps around the primary vortex. The secondary vortex structure is characterized by a loop of high-magnitude vorticity that attaches at two points to the front face of the cylinder boundary layer, but with a weak vorticity sheet spanning between the loop legs along its length. The two points at which the vortex loop attaches to the cylinder boundary layer coincide with nodes in the limiting surface streamlines, with foci of opposite sign rotation in the surface vortex lines, and with minima of the surface pressure distribution. The strength of the secondary vortex loop increases along its length when measured at a fixed time, with strength smallest near the loop nose and increasing toward the loop base. The vortex loop strength increases with addition of a positive axial free-stream velocity and decreases with addition of a negative axial free-stream velocity.

When a free-stream velocity is introduced normal to the cylinder axis, the form of the secondary vorticity field can exhibit dramatic changes. A case examined computationally in this paper has the same value of impact parameter as in the 'high impact parameter' case studied using flow-visualization experiments by Krishnamoorthy *et al.* (1999). We observe that the secondary vorticity in this case does not develop into a loop-like structure, but instead rolls up to form a vortex that is located just off the cylinder surface with vorticity oriented mostly in the azimuthal direction. The iso-surface of the secondary vorticity magnitude in this case has the appearance of a quasi-two-dimensional ridge of vorticity encircling the front half of the cylinder, which remains nearly attached to the cylinder all along the length of the vortex until the primary vortex approaches very close to the cylinder. The strength of the secondary vortex is observed to increase nearly linearly with time as vorticity is fed from the cylinder boundary layer.

Research support was provided by the US Army Research Office under grant number DAAH04-96-1-0081, with The University of Iowa. Thomas L. Doligalski is the program manager. Computer time was provided by the National Partnership

for Advanced Computational Infrastructure (San Diego, California) and the US Department of Defense High Performance Computing Center.

REFERENCES

Affes, H. & Conlisk, A. T. 1993 Model for rotor tip vortex–airframe interaction. Part 1: Theory. *AIAA J.* **31**, 2263–2273.

Affes, H., Conlisk, A. T., Kim, J. M. & Komerath, N. M. 1993 Model for rotor tip vortex–airframe interaction. Part 2: Comparison with experiment. *AIAA J.* **31**, 2274–2282.

Affes, H., Xiao, Z. & Conlisk, A. T. 1994 The boundary-layer flow due to a vortex approaching a cylinder. *J. Fluid Mech.* **275**, 33–57.

Affes, H., Xiao, Z., Conlisk, A. T., Kim, J. M. & Komerath, N. M. 1998 Model for rotor tip vortex–airframe interaction. Part 3: Viscous flow on airframe. *AIAA J.* **36**, 409–415.

Barker, S. J. & Crow, S. C. 1977 The motion of two-dimensional vortex pairs in a ground effect. *J. Fluid Mech.* **82**, 659–671.

Bi, N. & Leishman, J. G. 1990 Experimental study of rotor/body aerodynamic interactions. *J. Aircraft* **27**, 779–788.

Bi, N., Leishman, J. G. & Crouse, G. L. 1993 Investigation of rotor tip vortex interaction with a body. *J. Aircraft* **30**, 879–888.

Borouchaki, H. & Lo, S. H. 1995 Fast Delauney triangularization in three dimensions. *Comput. Meth. Appl. Mech. Engng* **128**, 153–167.

Brand, A., Komerath, N. M. & McMahon, H. 1989 Results from laser sheet visualization of a periodic rotor wake. *J. Aircraft* **26**, 438–443.

Brand, A. G., Komerath, N. M. & McMahon, H. M. 1990 Correlations of rotor wake/airframe interaction measurements with flow visualization data. *J. Am. Helicopter Soc.* **10**, 4–15.

Clarke, N. R. & Tutty, O. R. 1994 Construction and validation of a discrete vortex method for the two-dimensional incompressible Navier–Stokes equations. *Comput. Fluids* **23**, 751–783.

Dhanak, M. R. 1981 Interaction between a vortex filament and an approaching rigid sphere. *J. Fluid Mech.* **110**, 129–147.

Doligalski, T. L., Smith, C. R. & Walker, J. D. A. 1994 Vortex interaction with walls. *Ann. Rev. Fluid Mech.* **26**, 573–616.

Doligalski, T. L. & Walker, J. D. A. 1984 The boundary layer induced by a convected two-dimensional vortex. *J. Fluid Mech.* **139**, 1–28.

Gossler, A. A. 1999 A tetrahedral element Lagrangian vorticity method with application to vortex–cylinder interaction. PhD dissertation, University of Iowa, Iowa City.

Harvey, J. K. & Perry, F. J. 1971 Flow field produced by trailing vortices in the vicinity of the ground. *AIAA J.* **9**, 1659–1660.

Hess, J. L. & Smith, A. M. O. 1966 Calculation of potential flow about arbitrary bodies. *Prog. Aeronaut. Sci.* **8**, 1–138.

Kempka, S. N. & Strickland, J. H. 1993 A method to simulate viscous diffusion of vorticity by convective transport of vortices at a non-solenoidal velocity. Sandia Nat. Lab. Tech. Rep. SAND93-1763.

Kida, S. & Takaoka, M. 1994 Vortex reconnection. *Ann. Rev. Fluid Dyn.* **26**, 169–189.

Kim, J. M. & Komerath, N. M. 1995 Summary of the interaction of a rotor wake with a circular cylinder. *AIAA J.* **33**, 470–478.

Knio, O. M. & Ghoniem, A. F. 1990 Numerical study of a three-dimensional vortex method. *J. Comput. Phys.* **86**, 75–106.

Koumoutsakos, P., Leonard, A. & Pépin, F. 1994 Boundary conditions for viscous vortex methods. *J. Comput. Phys.* **113**, 52–61.

Krishnamoorthy, S., Gossler, A. A. & Marshall, J. S. 1999 Normal vortex interaction with a circular cylinder. *AIAA J.* **37**, 50–57.

Krishnamoorthy, S. & Marshall, J. S. 1998 Three-dimensional blade-vortex interaction in the strong-vortex regime. *Phys. Fluids* **10**, 2828–2845.

Liou, S. G., Komerath, N. M. & McMahon, H. M. 1990 Measurement of the interaction between a rotor tip vortex and a cylinder. *AIAA J.* **28**(6), 975–981.

Luton, A., Ragab, S. & Telionis, D. 1995 Interaction of spanwise vortices with a boundary layer. *Phys. Fluids* **7**, 2757–2765.

Marshall, J. S. 1997 The flow induced by periodic vortex rings wrapped around a columnar vortex core. *J. Fluid Mech.* **345**, 1–30.

Marshall, J. S. & Grant, J. R. 1996 Penetration of a blade into a vortex core: vorticity response and unsteady blade forces. *J. Fluid Mech.* **306**, 83–109.

Marshall, J. S. & Grant, J. R. 1997 A Lagrangian vorticity collocation method for viscous, axisymmetric flows with and without swirl. *J. Comput. Phys.* **138**, 302–330.

Marshall, J. S., Grant, J. R., Gossler, A. A. & Huyer, S. A. 2000 Vorticity transport on a Lagrangian tetrahedral mesh. *J. Comput. Phys.* **161**, 85–113.

Marshall, J. S. & Yalamanchili, R. 1994 Vortex cutting by a blade. Part II: Computations of vortex response. *AIAA J.* **32**, 1145–1150.

Melander, M. V. & Hussain, F. 1993 Coupling between a coherent structure and fine-scale turbulence. *Phys. Rev.* E **48**, 2669–2689.

Neves, J. C., Moin, P. & Moser, R. D. 1994 Effects of convex transverse curvature on wall-bounded turbulence. Part 1. The velocity and vorticity. *J. Fluid Mech.* **272**, 349–381.

Newman, J. N. 1986 Distributions of sources and normal dipoles over a quadrilateral panel. *J. Engng Maths* **20**, 113–126.

Ogami, Y. & Akamatsu, T. 1991 Viscous flow simulation using the discrete vortex model – the diffusion velocity method. *Comput. Fluids* **19**, 433–441.

Peace, A. J. & Riley, N. 1983 A viscous vortex pair in ground effect. *J. Fluid Mech.* **129**, 409–426.

Peridier, V. J., Smith, F. T. & Walker, J. D. A. 1991*a* Vortex-induced boundary-layer separation. Part 1. The unsteady limit problem. *J. Fluid Mech.* **232**, 99–131.

Peridier, V. J., Smith, F. T. & Walker, J. D. A. 1991*b* Vortex-induced boundary-layer separation. Part 2. Unsteady interacting boundary-layer theory. *J. Fluid Mech.* **232**, 133–165.

Perry, A. E. & Chong, M. S. 1987 A description of eddying motions and flow patterns using critical-point concepts. *Ann. Rev. Fluid Mech.* **19**, 125–155.

Rockwell, D. 1998 Vortex–body interactions: *Ann. Rev. Fluid Mech.* **30**, 199–229.

Salmon, J. K. & Warren, M. S. 1994 Skeletons from the treecode closet. *J. Comput. Phys.* **111**, 136–155.

Sheridan, P. F. & Smith, R. P. 1980 Interactional aerodynamics – a new challenge to helicopter technology. *J. Am. Helicopter Soc.* **25**, 3–21.

Tobak, M. & Peake, D. J. 1982 Topology of three-dimensional separated flows. *Ann. Rev. Fluid Mech.* **14**, 61–85.

Xiao, Z., Burggraf, O. R., & Conlisk, A. T. 1997 The interacting boundary-layer flow due to a vortex approaching a cylinder. *J. Fluid Mech.* **346**, 319–343.

Zienkiewicz, O. 1977 *The Finite Element Method*. McGraw-Hill.